GLIA

WILEY

RESEARCH ARTICLE

The formation of paranodal spirals at the ends of CNS myelin sheaths requires the planar polarity protein Vangl2

Andrew A. Jarjour[1] [ID] | Atanaska N. Velichkova[2] | Amanda Boyd[1] | Kathryn M. Lord[1] | Carole Torsney[2] | Deborah J. Henderson[3] | Charles ffrench-Constant[1]

[1]MRC Centre for Regenerative Medicine and MS Society/University of Edinburgh Centre for Translational Research, Scottish Centre for Regenerative Medicine, The University of Edinburgh, Edinburgh, UK

[2]Centre for Discovery Brain Sciences, The University of Edinburgh, Hugh Robson Building, Edinburgh, UK

[3]Institute of Genetic Medicine, Newcastle University, Centre for Life, Newcastle upon Tyne, UK

Correspondence
Andrew A. Jarjour, MSD UK Discovery Centre MRL, London Bioscience Innovation Centre, 2 Royal College Street, London NW1 0NH, UK.
Email: andrew.jarjour@merck.com

Funding information
Multiple Sclerosis Society; Wellcome Trust

Abstract

During axonal ensheathment, noncompact myelin channels formed at lateral edges of the myelinating process become arranged into tight paranodal spirals that resemble loops when cut in cross section. These adhere to the axon, concentrating voltage-dependent sodium channels at nodes of Ranvier and patterning the surrounding axon into distinct molecular domains. The signals responsible for forming and maintaining the complex structure of paranodal myelin are poorly understood. Here, we test the hypothesis that the planar cell polarity determinant Vangl2 organizes paranodal myelin. We show that Vangl2 is concentrated at paranodes and that, following conditional knockout of Vangl2 in oligodendrocytes, the paranodal spiral loosens, accompanied by disruption to the microtubule cytoskeleton and mislocalization of autotypic adhesion molecules between loops within the spiral. Adhesion of the spiral to the axon is unaffected. This results in disruptions to axonal patterning at nodes of Ranvier, paranodal axon diameter and conduction velocity. When taken together with our previous work showing that loss of the apico-basal polarity protein Scribble has the opposite phenotype—loss of axonal adhesion but no effect on loop–loop autotypic adhesion—our results identify a novel mechanism by which polarity proteins control the shape of nodes of Ranvier and regulate conduction in the CNS.

KEYWORDS
cell polarity, myelin, node of Ranvier, oligodendrocyte, paranode, Vangl2

1 | INTRODUCTION

Myelination in the CNS provides electrical insulation along the length of the sheath and enables rapid conduction by restricting the voltage-dependent sodium channels responsible for propagating action potentials to the small gaps between adjacent sheaths—the nodes of Ranvier. Together, these ensure that the action potential "jumps" from node to node, so generating rapid and energy efficient saltatory conduction (Huxley & Stampfli, 1949; Tasaki & Takeuchi, 1942). Myelin also provides metabolic support by enabling the transport of substrates for ATP generation by the citric acid cycle into the ensheathed axon (Fünfschilling et al., 2012). While tight apposition of myelin lamellae is essential for the proper functioning of the sheath (Boison, Bussow, Durso, Muller, & Stoffel, 1995), the noncompacted regions of

the myelin sheath also play a critical role in regulating conduction along, and providing metabolic support to, the axon. Noncompact myelin consists of specialized channels that are formed as the myelin sheath is compacted and oligodendroglial cytoplasm is extruded to the edges of myelinating processes (Figure 1a). While the cytoplasm-filled channels formed once wrapping and compaction is complete are continuous within the sheath, they are subdivided into functionally and molecularly distinct regions (reviewed by Simons, Snaidero, & Aggarwal, 2012). The channel at the leading edge of the myelinating process forms the adaxonal inner tongue that runs along the surface of the axon under the sheath. Here adaxonal myelin proteins including the transporter MCT1 and CNPase are required for long-term metabolic support of the axon (Lappe-Siefke et al., 2003; Lee et al., 2012). By contrast, the paranodal channels, so named because of their location abutting the node of Ranvier, are formed at the lateral edges of the myelinating process and form a tight spiral. When cut in cross section along the axon, the turns of the spiral give the appearance of a series of loops—the so-called paranodal loops (Figure 1b).
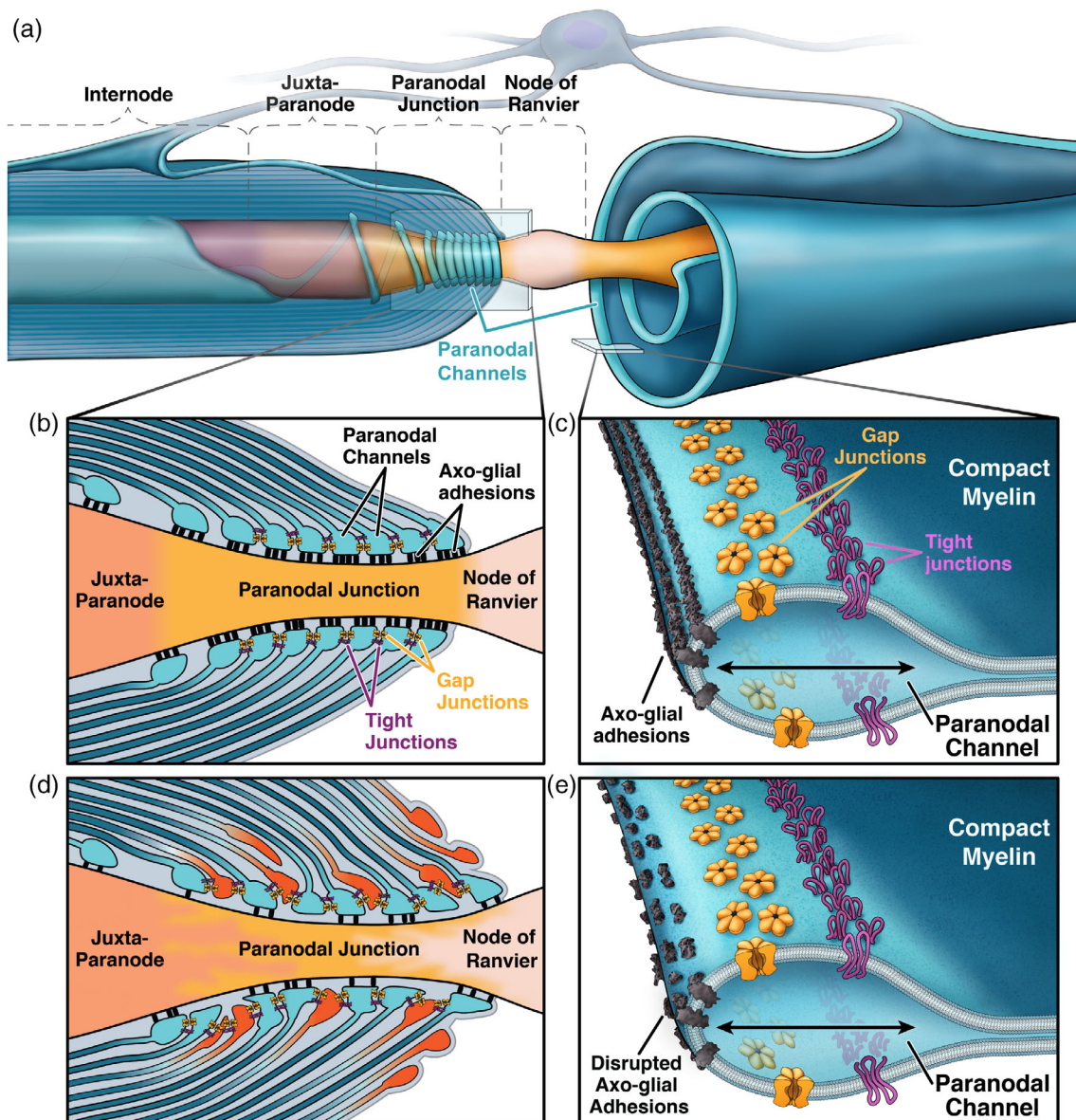

FIGURE 1 Organization of the CNS myelin sheath. (a) Myelin sheaths produced by oligodendrocytes consist of compacted layers of plasma membrane wrapped around the axon. The lateral edge of each sheath, which abuts the node of Ranvier (light pink) is characterized by a cytoplasm-filled channel that spirals around the paranodal axon (yellow), separating the node from the juxtaparanode (orange). The channel continues with a trajectory roughly parallel to the axon into the internodal axon (red). On the right is a partially unfurled myelin sheath, showing the division between compact myelin (dark blue) and the cytoplasmic channel (light blue). (b and c) A longitudinal cross section of the paranode reveals that the spiral appears as a series of cytoplasm-filled loops that are adhere to both the axon and each other. The adhesions present in each paranodal loops, and the polarity of the axis along which these adhesion complexes are patterned, are shown in c. (d and e) Paranodal axoglial adhesions are disrupted in the CNS following conditional elimination of *Scribble* expression in oligodendroglia [Color figure can be viewed at wileyonlinelibrary.com]

This paranodal spiral forms a close association with the underlying axon through an adhesion complex comprising the 155 kDa isoform of neurofascin (NFC155) on the oligodendrocyte binding to contactin-1 and Caspr on the axon (Charles et al., 2002; Rios et al., 2000). The resulting tight axoglial adhesion at the paranodal domain acts as a physical and electrical barrier separating the voltage-gated sodium channels required for saltatory conduction from the delayed rectifier potassium channels at the juxtaparanode (reviewed by Zollinger, Baalman, & Rasband, 2015). Another distinct set of adhesion proteins hold adjacent turns of the spiral together (so maintaining a tight spiral), including the tight junction protein Claudin-11 and gap junction protein Connexin-32 (Cx32), which are both essential for normal conduction in the CNS (Figure 1b, Devaux & Gow, 2008; Sargiannidou et al., 2009). These adhesion molecules are confined to lateral membranes of the channel, where they form autotypic junctions between neighboring paranodal loops (Gow et al., 1999; Kamasawa et al., 2005). While therefore essential for the complex three-dimensional organization and stability of the myelin sheath, the mechanisms responsible for the precise localization of the distinct sets of adhesion proteins within the paranodal channel and its resultant polarization (Figure 1c, arrow) are unknown.

The precise arrangement of axoglial and autotypic adhesions within the paranodal channel represents a remarkable example of subcellular polarization. In other cell types, the localization of proteins to specific membrane subdomains is controlled by evolutionarily conserved regulators of cell polarity. In epithelial cells, where the function of polarity proteins is best understood, this occurs along two perpendicular axes: Apico-basal polarity (ABP) signaling controls the distribution of proteins between the inner and outer faces of the epithelium, while the planar cell polarity (PCP) pathway operates in an orthogonal plane to the ABP pathway, conferring an "anterior" and "posterior" identity to lateral membranes within epithelial cells, and a directionality to the epithelium itself (reviewed by Campanale, Sun, & Montell, 2017). We have previously demonstrated that Scribble, a key regulator of ABP in epithelia (Bilder & Perrimon, 2000), is required for paranodal axoglial adhesion, as revealed by the detachment of loops from the axon following the conditional elimination of Scribble expression in oligodendroglia (Figure 1d,e; Jarjour et al., 2015). However, very little is known about the role played by the other major polarity signaling pathway, PCP, in CNS myelination. Among the highly evolutionarily conserved core PCP proteins, the four-pass transmembrane protein Van Gogh-like 2 (Vangl2), a vertebrate orthologue of *Drosophila* Van Gogh/Strabismus, is of particular interest owing to its close physical and functional interaction with Scribble (Courbard, Djiane, Wu, & Mlodzik, 2009; Montcouquiol et al., 2003; Yates et al., 2013). In neurons, Vangl2 has been implicated in the regulation of neurite outgrowth (Dos-Santos Carvalho et al., 2020), axon guidance (Leung et al., 2016; Sun, Purdy, & Walsh, 2016), dendritic spine morphology (Okerlund, Stanley, & Cheyette, 2016) and glutamatergic synapse formation (Thakar et al., 2017). It has previously been reported that the Vangl2 binding protein Prickle1 is expressed by oligodendroglia (Liu et al., 2013) and promotes their differentiation (Zilkha-Falb, Gurevich, Hanael, & Achiron, 2017), but the role played by Vangl2 itself in paranode formation and other oligodendroglial functions is unknown. Here, we have addressed this question by removing Vangl2 from oligodendrocytes. We reveal a striking phenotype in which the paranodal spiral loosens and unwinds and demonstrate that, as in epithelia, Vangl2 regulates the precise localization of junctional adhesion proteins. Within the paranodal spiral these adhesion proteins normally stabilize the paranodal channel in a tight spiral around the axon, a spiral that patterns the underlying axon. Thus, we reveal a novel role for PCP signaling molecules in both shaping and patterning the paranodal axon.

2 | MATERIALS AND METHODS

2.1 | Contact for reagent and resource sharing

Requests for further information, resources, and/or reagents should be addressed to Andrew Jarjour (andrew.jarjour@merck.com).

Reagents used:

Reagent or resource	Source	Identifier
Antibodies		
Mouse anti-pan Na$_V$	Sigma-Aldrich	Cat# S8809; RRID: AB_477552
Rabbit anti-Vangl2	Abcam	Cat# ab76174; RRID: AB_1925553
Mouse anti-Caspr	Antibodies, Inc.	Cat# 75-001; RRID: AB_2083496
Rabbit anti-Caspr	Abcam	Cat# ab34151; RRID: AB_869934
Chicken anti-NFH	BioLegend	Cat# 822601; RRID: AB_2564859
Rabbit anti-K$_V$1.1	Abcam	Cat# ab32433; RRID: AB_2265066
Rabbit anti-Claudin-11	Thermo Fisher	Cat# 36-4,500; RRID: AB_2533259
Mouse anti-Connexin-32 (IgG2a)	Thermo Fisher	Cat# 35-8,900; RRID: AB_87604
Rabbit anti-Septin-8	Proteintech	Cat# 11769-1-AP; RRID: AB_2185006

(Continues)

Reagent or resource	Source	Identifier
Mouse anti-βIV Spectrin (IgG2b)	Antibodies, Inc.	Cat# 75-377; RRID: AB_2315818
Mouse anti-βII Spectrin (IgG1)	BD Biosciences	Cat# 612563; RRID: AB_399854
Goat anti-MAG	Santa Cruz	Cat# sc-9,544; RRID: AB_670102
Rat anti-MBP	AbD Serotec	Cat# MCA409S; RRID: AB_325004
Goat anti-Vangl2	Abcam	Cat# ab60172; RRID: AB_946101
Rabbit anti-Prickle1	Proteintech	Cat# 22589-1-AP; RRID: N/A
Donkey anti-mouse IgG—Alexa Fluor 568	Thermo Fisher	Cat# A10037; RRID: AB_2534013
Donkey anti-rabbit IgG—Alexa Fluor 488	Thermo Fisher	Cat# A21206; RRID: AB_141708
Donkey anti-goat IgG—Alexa Fluor 647	Thermo Fisher	Cat# A21447; RRID: AB_141844
Donkey anti-chicken IgY—DyLight 405	Jackson Imm.	Cat# 703-475-155; RRID: AB_2340373
Goat anti-mouse IgG2a—Alexa Fluor 488	Thermo Fisher	Cat# A21131; RRID: AB_141618
Goat anti-rabbit IgG—Alexa Fluor 488	Thermo Fisher	Cat# A11008; RRID: AB_143165
Goat anti-mouse IgG1—Alexa Fluor 633	Thermo Fisher	Cat# A21126; RRID: AB_1500804
Goat anti-mouse IgG2b—Alexa Fluor 568	Thermo Fisher	Cat# A21144; RRID: AB_1500898
Donkey anti-rat IgG—Alexa Fluor 568	Abcam	Cat# ab175475; RRID: AB_2636887
Donkey anti-goat—Alexa Fluor 488	Thermo Fisher	Cat# A11055; RRID: AB_142672
Goat anti-CD140a (PDGFαR)	Biolegend	Cat#135902; RRID: AB_1953328
Anti-Griffonia Simplicifolia Lectin	Vector Labs	Cat# L-1100; RRID: AB_2336491
Bacterial and virus strains		
N/A		
Chemicals, peptides, and recombinant proteins		
Formaldehyde, 37% solution	Sigma-Aldrich	Cat# 252549
Glutaraldehyde, 25% solution	TAAB Laboratories	Cat# G011/2
Propylene oxide	Thermo Fisher	Cat# 10286460
Taab 812 premix kit-medium	TAAB Laboratories	Cat# T031
N-acetyl cysteine	Sigma-Aldrich	Cat# A9165
B27 supplement	Thermo Fisher	Cat# 17504-044
Biotin	Sigma-Aldrich	Cat# B4639
Trace elements B	Thermo Fisher	Cat# MT99175CI
Insulin, human recombinant	Simga-Aldrich	Cat# 91077C
Pen-strep-glu	Thermo Fisher	Cat# 10378
DMEM high glucose with Glutamax	Thermo Fisher	Cat# 31966-021
Sodium selenite	Sigma-Aldrich	Cat# S5261
Putrescine	Sigma-Aldrich	Cat# P5780
Forskolin	Sigma-Aldrich	Cat# F6886
Progesterone	Sigma-Aldrich	Cat#P8783
Apo-transferrin	Sigma-Aldrich	Cat# T1147
Bovine serum albumin	Sigma-Aldrich	Cat# A8806
Recombinant PDGF-AA	Peprotech	Cat# 100-13A;
Recombinant NT3	Peprotech	Cat# 450-03
Recombinant CNTF	Peprotech	Cat# 450-13
Poly-L-lysine	Sigma-Aldrich	Cat# P6282

(Continues)

Reagent or resource	Source	Identifier
Critical commercial assays		
gentleMACS dissociator	Miltenyi Biotec	130–093-235
Neural tissue dissociation kit (P)	Miltenyi Biotec	130–092-628
C tubes	Miltenyi Biotec	130–093-237
Experimental models: Organisms/strains		
Mouse: CNP[tm1(cre)Kan]	(Lappe-Siefke et al., 2003)	RRID: MGI: 3051754
Mouse: Vangl2 flox	(Ramsbottom et al., 2014)	N/A
Other		
Acupuncture needles, 25 mm long, 0.25 mm diameter	Journal of Chinese Medicine	Cat# NA3210
SuperFrost Plus slides	Thermo Fisher	Cat# 10149870

2.2 | Experimental model and subject details

Mice in which the *Vangl2* gene was targeted for condition elimination by insertion of LoxP sites flanking exon 4 (Ramsbottom et al., 2014) were crossed with mice expressing Cre recombinase under the control of the *2′-3′ cyclic nucleotide phosphodiesterase* (CNP) gene (Lappe-Siefke et al., 2003) to generate *CNP[+/Cre]:Vangl2^{fl/fl}* mice, in which *Vangl2* expression is conditionally eliminated in myelinating glia. Both male and female mice (1–8 weeks of age) were used. A total of 110 mice were used for all studies described in this study. All animal work conformed to UK legislation (Scientific Procedures) Act 1986 and to the University of Edinburgh regulations.

2.3 | Method details

2.3.1 | Mouse oligodendroglial cultures

Eight postnatal Day 7 mouse pups were killed by injection with a 1:1 mix of Dormitor and Vetelar and their cortices removed. Cortices were dissociated using a gentleMACS dissociator using C tubes with the Neural Tissue Dissociation Kit (Miltenyi Biotec). Cell suspensions were subjected to immunopanning, first by negative selection using "bacterial" (untreated) culture plates coated with anti-Griffonia Simplicifolia Lectin, then by positive selection using antibodies against platelet-derived growth factor receptor α (PDGFRα). Positively selected cells were cultured on PDL-coated T-75 flasks in OPC-Sato medium (high-glucose DMEM with, 1% apo-Transferrin, 1% bovine serum albumin, 9.934 mM Putrescine dihydrochloride, 19.88 μM progesterone, 0.2313 μM sodium selenite, B27 supplement, 0.3678 mM N-acetyl cysteine, 5 μg/ml insulin, Trace Element B mix, 4.093 nM biotin and 5 nM forskolin) with 10 ng/ml PDGF-AA and 5 ng/ml neurotrophin 3 (NT3) at 37°C in 7.5% CO_2. 50% medium changes were carried out every day for 7 days to allow OPCs to proliferate. When OPCs reached confluence, cells were seeded on PDL-coated 22 mm glass coverslips, and differentiated into oligodendrocytes in OPC-Sato medium with 5 ng/ml NT3 and 10 ng/ml ciliary neurotrophic factor (CNTF) for at 37°C in 7.5% CO_2 for 2 days. For immunocytochemical analyses, cultures were fixed with 4% paraformaldehyde and washed twice in PBS, and blocked with blocking solution (4% heat-inactivated donkey serum, 2% BSA, and 0.1% Triton X-100 in PBS). Cultures were incubated overnight in primary antibodies diluted in blocking solution. Following repeated washes with PBS, cultures were incubated with secondary antibodies, washed with PBS, and then mounted. Confocal z-stacks were acquired using Leica SP8 inverted confocal microscope (×63 objective, zoom 2). Images were processed using ImageJ and Photoshop (Adobe) software.

2.3.2 | Teased spinal cord fibers

Thirty-four postnatal Day 14 or 60 mice were fixed by cardiac perfusion with 4% formaldehyde in PBS. The cervical spinal cord was dissected out, and postfixed for 30 min in cold 4% formaldehyde in PBS before being stored in PBS at 4°C for at most 48 hr. The meninges were removed, and the ventral white matter isolated into cold PBS, and cut into pieces roughly 2 mm long. Fibers were then teased onto SuperFrost Plus slides (for standard confocal imaging) or TESPA-coated coverslips (for gSTED super-resolution imaging) using acupuncture needles. Slides were stored at −20°C in airtight containers until immunolabeling. Immunohistochemical labeling was carried out as described above for cultures. For standard confocal imaging, z-stacks were acquired using Leica SP8 inverted confocal microscope (×63 objective, 1.40 N.A.). Maximum intensity projection images of Z-stacks were used for analysis. Images were processed using ImageJ and Photoshop (Adobe) software. For immunolabeling of STED images, the secondary antibodies used were Atto647N-conjugated goat anti-rabbit IgG for Claudin-11 immunolabeling and Alexa 568-conjugated goat anti-mouse IgG (H + L) for Caspr labeling. For STED images, z-stacks were acquired using a Leica TCS SP8 STED ×3 microscope (×100 objective, 1.40 N.A.), using the 775 nm laser for depletion. Stacks were deconvolved using the Huygens STED deconvolution package (Scientific Volume Imaging B.L., Netherlands) integrated in Leica LAS AF software prior to analysis.

2.3.3 | Transmission electron microscopy

Forty-two postnatal Day 14 or 60 mice were fixed by cardiac perfusion with 4% formaldehyde/2.5% glutaraldehyde in 0.1 M phosphate buffer, pH 7.3. Samples were postfixed in 4% formaldehyde/2.5% glutaraldehyde in 0.1 M phosphate buffer, pH 7.3, for 2 hr, then in 1% glutaraldehyde in 0.1 M phosphate buffer for 14 days, washed in PBS and postfixed in 1% Osmium Tetroxide in 0.1 M phosphate buffer for 60 min. The samples were then dehydrated in increasing concentrations of ethanol and embedded in epoxy resin. Sections, 1 μm thick, were cut on a Reichert OMU4 ultramicrotome (Leica Microsystems), stained with Toluidine Blue and viewed in a light microscope to select suitable areas for investigation. 60 nm ultrathin sections were cut from selected areas, stained in Uranyl Acetate and Lead Citrate and then viewed using a JEOL JEM-1400 Plus transmission electron microscope. Images were acquired using a Gatan OneView camera (Gatan).

2.3.4 | Recording of compound action potentials

Following decapitation under isoflurane anesthesia, optic nerves from a total of 26 postnatal Day 60 mice were dissected free into oxygenated ice-cold dissection solution. The nerves were incubated for 1 hr in 36–37°C oxygenated recovery solution prior to transfer to a recording chamber continuously perfused with oxygenated Krebs' solution (1–2 ml/min) at room temperature. The oxygenated Krebs' solution contained (in mM) 125 NaCl, 2.5 KCl, 1.25 NaH_2PO_4, 26 $NaHCO_3$, 25 glucose, 1 $MgCl_2$, and 2 $CaCl_2$, pH 7.4. The recovery solution was identical to Krebs' solution apart from 1.5 $CaCl_2$ and 6 $MgCl_2$. Dissection solution was the same as the recovery solution with added 1 mM kynurenic acid.

Two glass suction electrodes were used to record compound action potentials, one for electrical stimulation and the second for recording compound action potentials (CAPs). The optic nerves were stimulated ×3 at 0.2 Hz (0.1 ms duration) with an ISO-flex stimulus isolator (A.M.P.I Intracel). The applied stimulation intensities were 1, 2.5, 5, 7.5, 10–50 (in steps of 5 μA), 60–100 (in steps of 10 μA), and 125–500 μA (in steps of 25 μA). The CAPs are composed of three main components that could be differentiated on the basis of activation threshold and conduction velocity, each displaying a characteristic triphasic (positive–negative–positive) responses that overlap (Figure 5a). Data were acquired and recorded using a Cygnus ER-1 differential amplifier (Cygnus Technologies, Inc.) and pClamp 10 software (Molecular Devices). Data were filtered at 10 kHz and sampled at 50 kHz.

2.4 | Quantification and statistical analyses

All confocal and TEM images were analyzed using FiJi software (Schindelin et al., 2012). For analysis of separation between paranodal loops, neighboring loops were considered separated if they were clearly separated by more than one membrane width for at least one-third of the length of the border between the loops. For analysis of detachment

of paranodal loops from the axon, a loop was considered detached if a separation of at least 100 nm was measured between the loop and axon. G-ratio was determined by dividing axon diameter by the total diameter of the axon and overlying myelin sheath. Axon diameter was calculated from measured axon perimeter based on an assumption of circularity. For measurements taken from optic nerve, the diameter of the myelinated axon was determined similarly. For measurements of g-ratio in spinal cord, where myelin sheaths often appeared uncompacted, myelin sheath thickness was measured directly at the point at which the myelin sheath was most compact, and myelinated axon diameter was determined by adding this value to the calculated axon diameter. Internodal axonal diameter was measured at the location in the field where the internodal axon was thickest. Paranodal axonal diameter was measured at the innermost border of whichever second loop from the inside is located closer to the node (where inner means toward the internode).

For analyses of trailing paranodal domains, a paranode was scored as trailing if either four or more turns of Caspr spiral or a 2 μm or longer continuous region of Caspr immunolabeling separated from the paranodal Caspr domain were visible within 20 μm from the juxtaparanodal end of the continuous paranodal Caspr-immunopositive domain. For analyses of the separation between axonal domain markers at nodal regions, the shortest distance along the axon between the edge of one domain and the other was measured. When these domains contacted each other or overlapped, the distance was measured as 0. For measurements of the width of axonal domains, the distance measured was the maximal distance along the axon where continuous immunoreactivity could be observed.

For gSTED analysis of immunofluorescence intensity of Claudin-11 or Caspr labeling, image stacks were cropped to eliminate half the paranodal spiral so that "top" and "bottom" edges of each turn of the spiral were not double-counted and a maximum intensity projection was performed. On the projected image, a 2 pixel-wide line was drawn longitudinally across the paranodal spiral starting at the nodal end and an intensity plot was generated. Maxima and minima were identified using the BAR Scripts 1.5.1 "Find Peaks" macro (Ferreira et al., 2017).

Clampfit 10.7.0.3 was used for analyzing the CAP recordings. The activation threshold for each component was defined as the lowest stimulation intensity at which the negative component of the triphasic response was clearly identifiable. The conduction velocity was calculated based on the latency to the negative peak of each component at 100 μA. Group comparisons were made using two-way ANOVA followed by Sidak's multiple comparisons test.

Statistical analyses were performed using GraphPad Prism. Descriptions of statistical analyses performed are provided in the figure legends. All data are presented as mean ± *SEM*.

3 | RESULTS

3.1 | Vangl2 is expressed by oligodendroglia and is localized to CNS paranodes

To ask whether Vangl2 plays a role in organizing the myelin sheath, we first examined its distribution within oligodendroglia and in CNS

myelin. We confirmed that Vangl2 is expressed by MBP-positive oligodendroglia. Vangl2 is localized to cell bodies and processes in wild-type oligodendrocytes but is excluded from myelin-like membrane sheets (Figure 2a,b). It is localized predominantly to Caspr-immunolabeled paranodes in teased spinal cord preparations from postnatal Day 60 (P60) spinal cord, although some internodal Vangl2 labeling was also observed (Figure 2e,f). We observed a similar distribution of the Vangl2 binding partner Prickle1 in both cultured oligodendrocytes (Figure S1A–C), and in P60 teased spinal cord preparations (Figure S1D,E).

To confirm that the paranodal immunolabeling represented Vangl2 expression in oligodendrocytes, and to enable the further studies below, we conditionally eliminated Vangl2 expression from myelinating glia by creating _Vangl2_ cKO (_CNP^+/Cre_:_Vangl2^fl/fl_) mice. Conditional elimination of Vangl2 in these oligodendroglia was verified in purified cultures derived from Vangl2 cKO cortex (Figure 2c,d),

where Vangl2 immunolabeling was substantially decreased relative to that observed in Vangl2 WT (_CNP^+/+_:_Vangl2^fl/fl_) oligodendroglia (Figure 2a,b). Importantly, immunolabeling of teased axons from the mice showed that paranodal Vangl2 was absent from Vangl2 cKO paranodes (Figure 2g,h) relative to Vangl2 WT paranodes (Figure 2e, f), confirming that the Vangl2 present at CNS paranodes is expressed by oligodendrocytes and not by the underlying axon.

3.2 | Oligodendroglial Vangl2 organizes CNS paranodes and nodes of Ranvier

Our previous findings demonstrated that the apico-basal polarity protein Scribble is required for normal CNS myelin initiation, thickness and paranodal axoglial adhesion (Jarjour et al., 2015). By contrast, Vangl2 cKO animals had no reduction in the proportion of myelinated
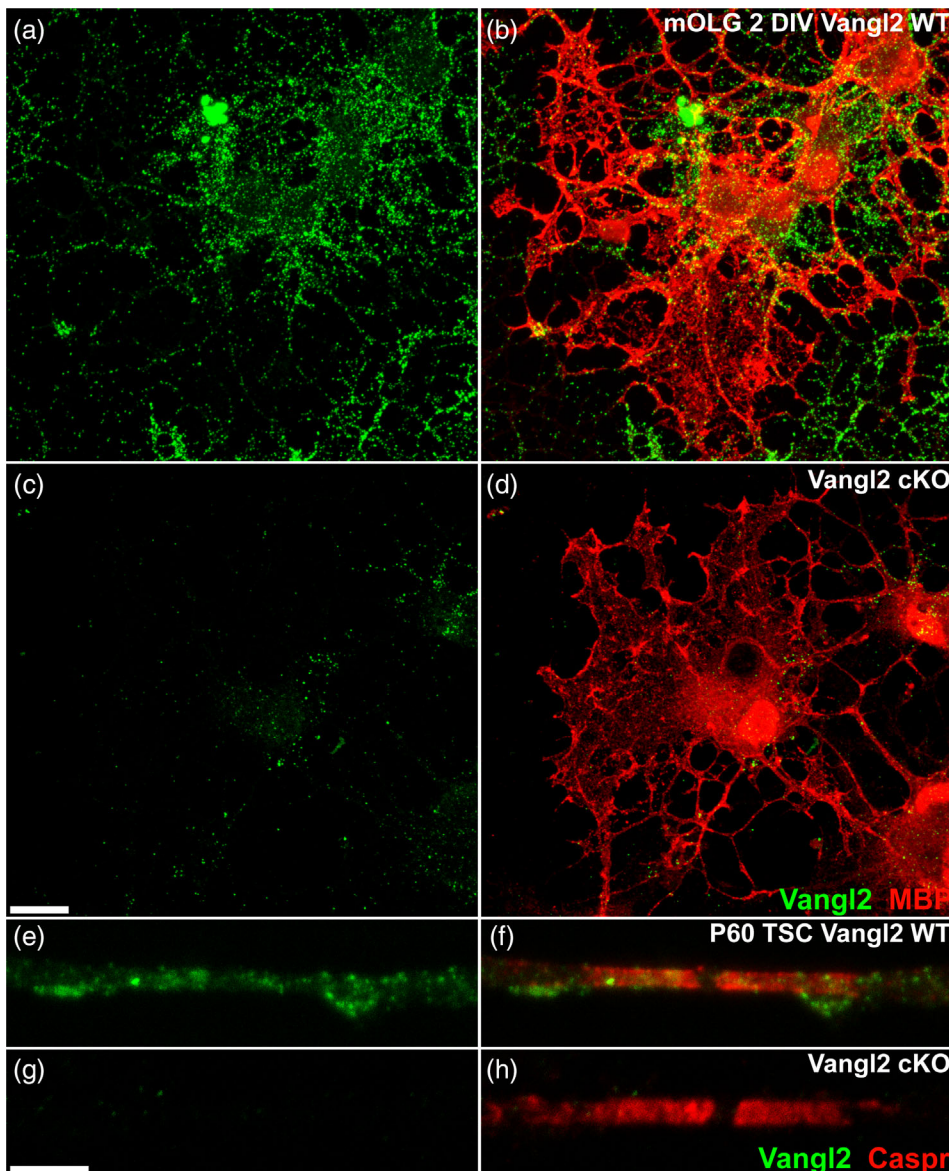

FIGURE 2 Elimination of Vangl2 expression in CNP-Cre:Vangl2^fl/fl oligodendrocytes and paranodes. Cultures derived from Vangl2 WT mice and differentiated for 2 days show expression of Vangl2 protein (a and b, green) by oligodendrocytes expressing myelin basic protein (MBP, b, red). Vangl2 protein is almost entirely absent from oligodendrocyte cultures derived from Vangl2 cKO mice (c and d). Similarly, Vangl2 protein (e and f, green) is present at paranodes labeled for Caspr (f, red) in P60 teased spinal cord fibers from Vangl2 WT mice, but not in teased fiber preparations from Vangl2 cKO mice (g and h). Scale bars: (a–d): 5 μm, (e–h): 3 μm [Color figure can be viewed at wileyonlinelibrary.com]
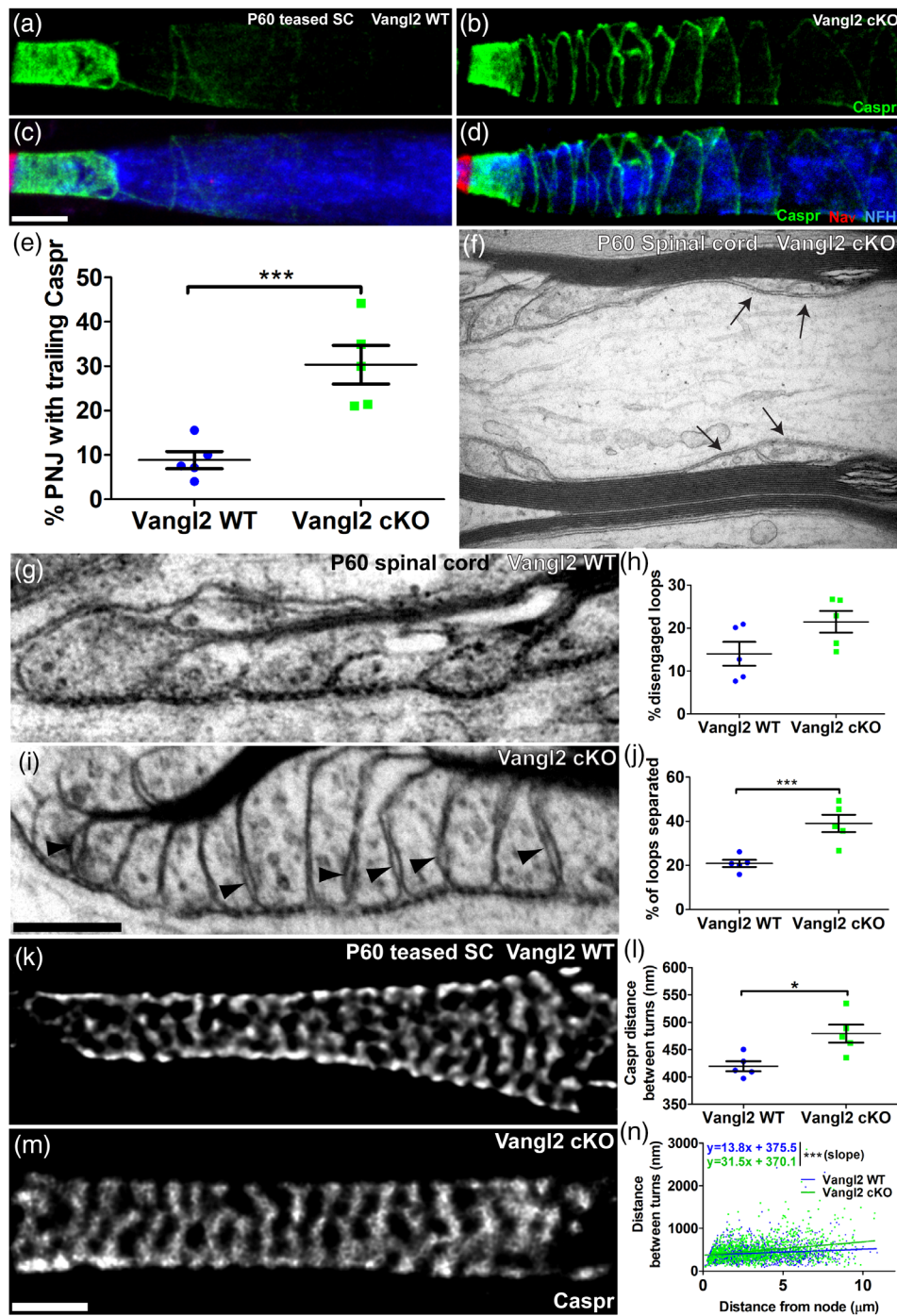
FIGURE 3 Disruption of the paranodal spiral in the Vangl2 conditional mutant CNS. (a–d) The paranodal spiral is disrupted in Vangl2 cKO CNS. Caspr immunolabeling (green) extends away from NaV immunolabeling (red), into the internode in Vangl2 cKO CNS (b and d), forming a looser (trailing) spiral than observed in wild-type controls (a and c). Note that the portion of the paranodal spiral closest to the node remains tightly wound, as evidenced by solid Caspr immunostaining. In panels c and d, the axon is immunolabeled for the 200 kDA neurofilament subunit (NFH, blue). The percentage of these paranodes with trailing Caspr was significantly increased (e, WT: 8.8 ± 1.9, cKO: 30.3 ± 4.4, p = .0079). (f) Electron microscopy reveals the presence of aberrant cytoplasm-filled myelin loops in internodal myelin in Vangl2 cKO spinal cord at P60 (f, arrows). (g–j) Paranodal loops largely remain adhered to the axonal surface in the Vangl2 cKO CNS (i), as in wild-type CNS (g, quantification in h, Percentage of paranodal loops disengaged from the axonal surface: WT: 14.0 ± 2.8, cKO: 21.6 ± 2.4, p = .0952). An increase in the percentage of paranodal loops that were separated from each other was observed in Vangl2 cKO spinal cord (i, arrowheads), relative to wild-type (g, quantification in j, Percentage of interfaces between neighboring paranodal loops showing separation: WT: 20.9 ± 1.6, cKO: 39.0 ± 4.0, p = .0079). (k–n) Super-resolution gSTED confocal imaging of the Caspr spiral further revealed that spacing between turns of the paranodal spiral is increased in Vangl2 cKO teased spinal cord fibers at P60 (m) relative to wild-type paranodes (k, quantification in l and n; Mean distance between turns of the paranodal spiral: WT: 419.5 ± 9.2 nm, cKO: 479.2 ± 16.4 nm, p = .016; Equation of best-fit line: WT: y = 13.8 ± 2.5x + 375.5 ± 10.0, cKO: y = 31.5 ± 3.1x + 370.1 ± 13.4, p < .0001 [slope]). All data are represented as mean ± *SEM*. n = 5 mice per genotype. Statistical analyses were performed using the Mann–Whitney test. (a–e) At least 40 paranodes were analyzed per animal. g–k, k–n: At least 20 paranodes were analyzed per animal. Scale bars (a–d): 5 μm, (g and i): 250 nm, (k and m): 1 μm [Color figure can be viewed at wileyonlinelibrary.com]
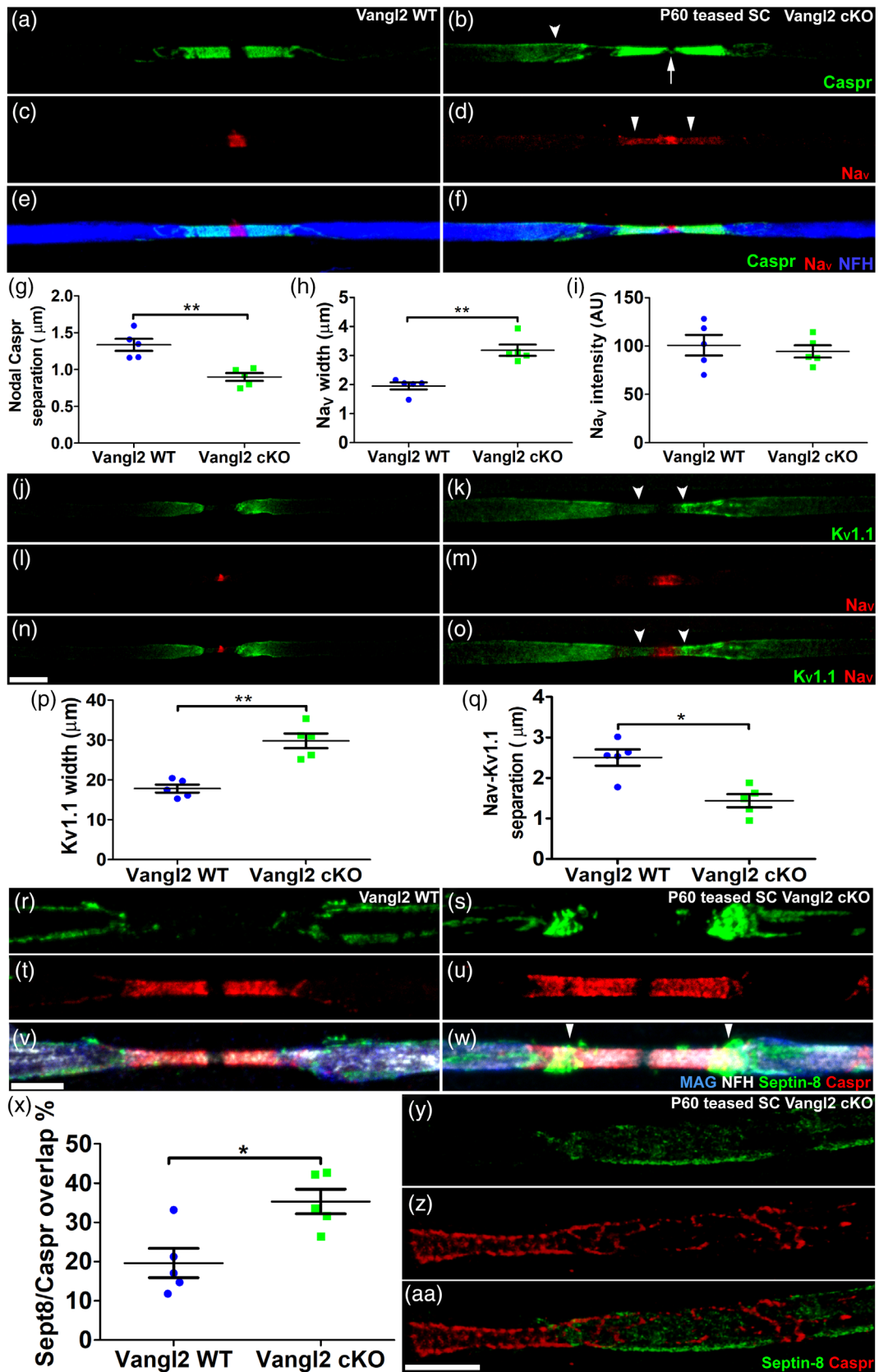
FIGURE 4 Legend on next page.

axons in P14 optic nerve (Figure S2A–D) nor any change in g-ratio in P60 spinal cord (Figure S2E–H), suggesting that Vangl2 does not regulate myelin sheath formation or wrapping in the CNS. To assess paranodal architecture, we examined the distribution of the axonal molecule Caspr, part of the axoglial adhesion complex that marks sites of axon-loop contact. Normally, the tight apposition of paranodal loops to one another means that, using immunofluorescent light microscopy, the Caspr spiral appears as a uniform band, as was observed in P60 teased fiber preparations from Vangl2 WT spinal cord (Figure 3a,c). In the Vangl2 cKO, however, paranodal organization was disrupted as evidenced by the loosening of the Caspr spiral. An increased proportion of Vangl2 cKO paranodes display loops that extend back within the internode as a loose spiral (Figure 3b,d, quantification in e). In some cases, the interruption between paranodal loops was observed as a split between the loops closest to the node and those trailing back into the internode (Figure 3f, arrows). In contrast to our observations in CNS myelin lacking Scribble, we did not observe a significant increase in disengagement of paranodal loops from the axonal surface in Vangl2 cKO spinal cord at P60 using transmission electron microscopy (TEM, Figure 3h). However these TEM studies did show that, even when no obvious differences in the "tightness" of the paranodal spiral in regions closest to the node could be observed in Vangl2 cKO teased fibers using standard confocal imaging, a significantly increased proportion of neighboring paranodal loops were separated (Figure 3g,i [arrowheads], j).

To ask whether this loosening of the paranodal spiral seen at P60 reflects a failure of the formation of the paranodal structure or a loss of its maintenance once formed, we analyzed P14 spinal cord—a time when axons are still growing in length. Here we found using EM that slight separations between loops could be seen even at this early time point (Figure S3), although statistical significance was not reached until the axons lengthened at P60. We conclude, therefore, that Vangl2 is required for normal adhesion between paranodal loops in the CNS, with the consequent phenotype of a loosened spiral fully revealed once the axon has lengthened. Vangl2 is not, however, required for the adhesion between loops and axon.

To further quantify the spacing between turns of the paranodal spiral, paranodal Caspr immunolabeling was imaged using super-resolution gated STED (gSTED) confocal microscopy. The distance between turns of the Caspr spiral, measured by determining the distance between Caspr intensity peaks, was increased at Vangl2 cKO paranodes (Figure 3m) relative to wild-type paranodes (Figure 3k, quantified in L). Increased spacing between loops became more pronounced with distance from the node of Ranvier, as visualized by the increase in slope of the best-fit line when plotting distance between turns against distance from the node of Ranvier (Figure 3n).

3.3 | Vangl2 organizes the CNS myelin sheath and patterns the underlying axon

Two of the key functions of CNS paranodal axoglial adhesions are to promote the concentration of an axolemmal protein complex containing voltage-gated sodium (Na_V) channels at nodes of Ranvier (Zonta et al., 2008), and to form a barrier that separates the nodal complex from a juxtaparanodal complex containing voltage-gated potassium (K_V) channels(Bhat et al., 2001). To determine whether paranodal function was disrupted in the absence of Vangl2 expression by oligodendroglia, we examined axonal organization in teased spinal cord preparations from P60 Vangl2 cKO mice. We observed that, while Caspr-immunolabeled paranodes flank Na_V-immunopositive nodes of Ranvier in wild-type CNS (Figure 4a,c,e), paranodal Caspr extends into the nodes of Ranvier of the Vangl2 cKO mice, narrowing the nodal "gap" between neighboring paranodes (Figure 4b [arrow], f,g), and also in toward the internode (Figure 4b, arrowhead). Reduced distance across the node of Ranvier could also be detected by TEM in P60 spinal cord (Figure S4). Surprisingly, despite the narrowing of the node of Ranvier in the Vangl2 cKO CNS, the nodal Na_V-immunolabeled domain was widened, with Na_V labeling extending laterally into the paranodes (Figure 4d [arrowheads], f,h) with no significant difference in the mean intensity of nodal Na_V immunofluorescence observed in Vangl2 cKO teased spinal cord at P60 (Figure 4i). This widening of the Na_V-labeled

FIGURE 4 Oligodendroglial Vangl2 expression is required for domain organization of myelinated CNS axons at nodes of Ranvier. In wild-type CNS, Caspr-immunopositive paranodes (green) flank Na_V-immunopositive nodes of Ranvier (red), with a clear separation existing between neighboring paranodes (a, c, and e). In Vangl2 cKO CNS (b, d, and f) the Caspr domain extends both into the internode (b, arrowhead) and into the node of Ranvier (b, arrow). This shortens the node (quantified in g, distance between paranodal Caspr immunolabeling across node of Ranvier (μm): WT: 1.34 ± 0.08, cKO: 0.90 ± 0.05, p = .0079). The nodal Na_V-immunolabeled domain is widened and spreads laterally into the paranodes (d, arrowheads, quantified in h; width of nodal Na_V immunolabeling (μm): WT: 1.9 ± 0.1, cKO: 3.2 ± 0.2, p = .0079). No significant change in nodal sodium channel immunolabeling intensity was observed in Vangl2 cKO CNS (i; WT: 100.8 ± 10.6, cKO: 94.4 ± 6.4, p = .8413). In wild-type CNS, a clear paranodal separation is observed between nodal Na_V (red) and juxtaparanodal K_V (green) immunolabeling (j, l, and n). In Vangl2 cKO (k, m, and o), the K_V-immunolabeled area is widened (p; width of K_V1.1 immunolabeling (μm): WT: 17.8 ± 1.0, cKO: 28.9 ± 3.2, p = .0079) and invades the paranodal domain (k and o, arrowheads), with the distance between Na_V and K_V1.1 immunolabeling reduced (q; WT: 2.5 ± 0.2 μm, cKO: 1.5 ± 0.2 μm, p = .0159). (q–aa): Septin-8 is mislocalized to paranodes in Vangl2 cKO P60 teased spinal cord fibers. Septin-8 (green), which is restricted to the internodal inner tongue in wild-type fibers (r, t, and v), extends into Caspr-immunopositive (red) paranodal regions in Vangl2 cKO fibers (s, u, and w, arrowheads), with the percentage length of the Caspr-immunopositive domain that overlapped with Septin-8 labeling being significantly increased (x; WT: 19.6 ± 3.7, cKO: 35.3 ± 3.1, p = .0317). Myelin was immunolabeled for MAG (blue) and axons for NFH (white). Super-resolution imaging using gated STED reveals that Septin-8 (green, y, aa) and Caspr (red, z, aa) do not colocalize at paranodes. All data are represented as mean ± SEM. n = 5 mice per genotype. Statistical analyses were performed using the Mann–Whitney test. a–h: At least 20 nodes of Ranvier were analyzed per animal. i–p: At least 40 paranodes were analyzed per animal. Scale bars: (a–f and j–o): 5 μm, (y–aa): 300 nm [Color figure can be viewed at wileyonlinelibrary.com]

domain in Vangl2 cKOs was observed in all rather than a subset of nodes, and was not dependent on axon diameter (data not shown).

We also observed a similar change when we examined the distribution of axonal spectrins at Vangl2 cKO nodes of Ranvier. The mutual exclusion of the βIV spectrin-containing nodal cytoskeleton (Figure S5A,E) and the βII spectrin-containing complex underlying the paranodal cytoskeleton (Figure S5C,E) is a key mediator of the paranode's Na$_V$ clustering and barrier functions(Amor et al., 2017). We observed that in Vangl2 cKO CNS, the width of nodal βIV spectrin domains were widened (Figure S5B,F,H), while the distance across the nodal gap in βII spectrin labeling was decreased (Figure S5D,F,G), mirroring the changes in Caspr and Na$_V$ distribution observed in these animals. The observation that axonal nodal and paranodal protein complexes and their underlying cytoskeleta are mislocalized in Vangl2 cKO CNS shows that oligodendroglial Vangl2 is essential to maintain the separation between axonal nodal and paranodal domains in the CNS.

Next, we investigated whether Vangl2 plays a role in regulating the border between the paranodal and juxtaparanodal domains. While we observed a clear paranodal separation between immunolabeling for juxtaparanodal K$_V$1.1 (Figure 4j,n) and nodal Na$_V$ (Figure 4l,n) in wild-type CNS, the K$_V$1.1 immunopositive domain was widened in Vangl2 cKO CNS (Figure 4k,o,p), where it invaded paranodes, reducing the distance measured between Na$_V$ and K$_V$1.1-labeled domains (Figure 4o [arrows], q). These data indicate that Vangl2 is essential for maintaining the paranodal "barrier" between the juxtaparanodal and

nodal domains in the CNS. Notably, these findings diverge from our previous observation of a similar disruption of paranodal barrier function in mice lacking oligodendroglial Scribble expression(Jarjour et al., 2015) in that in the Scribble cKO mice axoglial adhesion of the paranodal loops is disrupted, while the disruption of axonal patterning in Vangl2 cKO CNS occurs despite the presence of largely intact paranodal axoglial adhesion. We can therefore conclude that polarity proteins Vangl2 and Scribble act through different mechanisms at CNS paranodes.

Finally, we examined the transition between the internodal and paranodal domain by examining the distribution of Septin-8, a component of the septin cytoskeleton that is restricted to the innermost wrap of internodal myelin (Patzig et al., 2016). In teased fiber preparations from wild-type spinal cord, we typically observed a clear separation between internodal Septin-8 and paranodal Caspr labeling (Figure 4r,t,v), with the former restricted to the leading edge (or inner tongue) of the myelin sheath while the latter is present only in the lateral cytoplasmic channels that for the paranodal spiral. In Vangl2 cKO fibers, however, there was a significant increase in the proportion of paranodes at which Septin-8 immunolabeling invaded the paranodal domain (Figure 4s,u,w [arrowheads], x). A closer examination using gated STED (gSTED) super-resolution confocal microscopy indicated that while Septin-8 labeling was interspersed with that for Caspr in the paranodal spirals of the Vangl2 cKO fibers, their distribution did not overlap (Figure 4x–aa). The invasion of the paranodal spirals in these mutants by an internodal noncompact myelin protein is
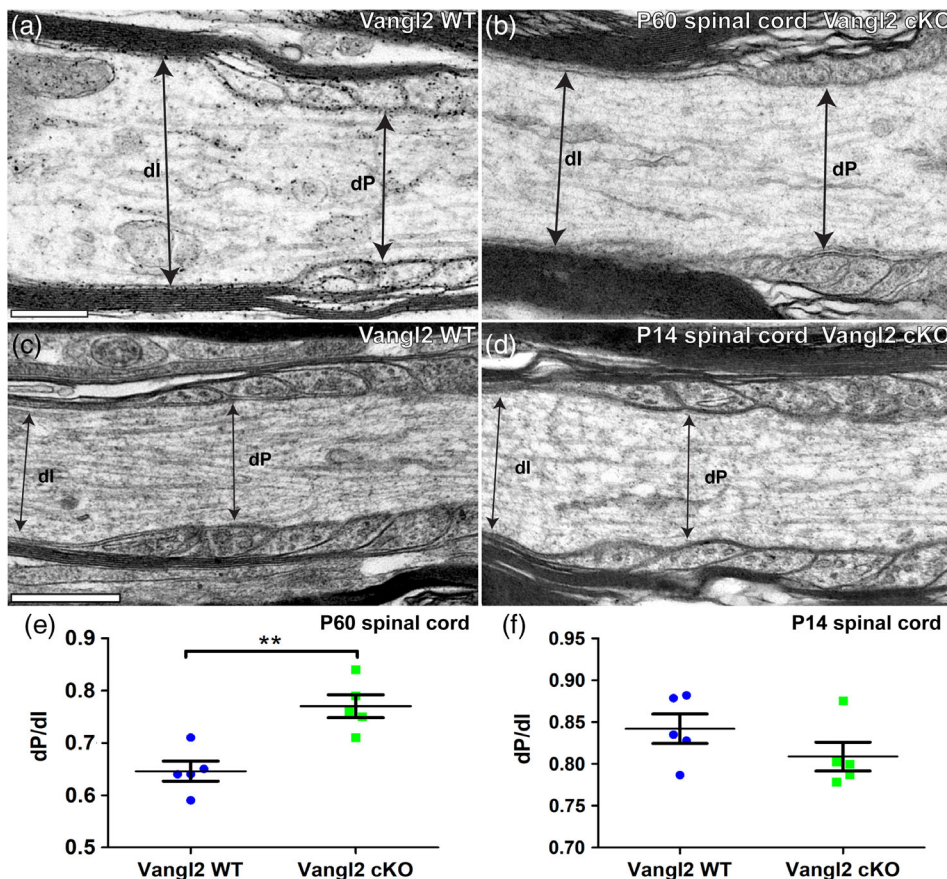

FIGURE 5 Vangl2 is required for local regulation of axon diameter in myelinated CNS axons. In wild-type spinal cord at P60 (a), paranodal axon diameter (dP) is smaller than internodal diameter (dI). A relative increase in dP is observed in Vangl2 cKO spinal cord at P60 (b), resulting in an increased dP/dI ratio relative to that observed in wild-type controls (e; WT: 0.73 ± 0.02, cKO: 0.77 ± 0.02, p = .0157). dP/dI ratio is not significantly different between Vangl2 WT and cKO in P14 spinal cord (c, d, and f; WT: 0.84 ± 0.02, cKO: 0.81 ± 0.02, p = .2222). All data are represented as mean ± *SEM*. n = 5 mice per genotype. Statistical analyses were performed using the Mann–Whitney test. At least 25 paranodes were analyzed per animal, per time point. Scale bars: (a and b) and (c and d): 500 nm [Color figure can be viewed at wileyonlinelibrary.com]

consistent with Vangl2 also playing an important role in the functional division between internodal and paranodal noncompact myelin.

## 3.4 | Vangl2 is required for local regulation of axon diameter at CNS paranodes

In addition to patterning the underlying axon into distinct molecular domains, the myelin sheath physically shapes the axon. Contact between oligodendrocytes and axons promotes radial axonal growth during development (Sanchez, Hassinger, Paskevich, Shine, & Nixon, 1996), with the internodal axon diameter being greater than that of the paranode and node in the adult CNS (Hildebrand & Skoglund, 1971). When the ratio of paranodal axon diameter (dP) to internodal axon diameter (dI) was measured in Vangl2 cKO spinal cord at P60, an increased dP/dI ratio relative to that observed in wild-type spinal cord (Figure 5a,b,e) was observed. Interestingly, this difference between Vangl2 cKO and WT axons was not seen in P14 spinal cord, a stage at which axons are still increasing in diameter (Figure 5c,d,f). We

conclude that oligodendroglial Vangl2 is essential for the local regulation of axon diameter at CNS paranodes.

3.5 | Increased conductivity in Vangl2 cKO CNS

The observed disruptions to axonal domain organization and the regulation of axon diameter at nodal regions in the Vangl2 cKO raised the question of how these changes, particularly to the length and diameter of the node of Ranvier, affect conduction. When compound action potentials (CAPs) were measured in the optic nerve at P60, we observed three peaks (Figure 6a, arrowhead, black arrow, gray arrow), as has previously been reported (Foster, Connors, & Waxman, 1982). Across all three peaks, conduction velocities were increased in Vangl2 cKO nerves compared to wild-type controls (Figure 6b). Further analysis revealed that the minimum stimulus intensity required to elicit each component of the CAP was decreased in Vangl2 cKO nerves (representative traces shown in Figure 6c, quantification in Figure 6d). These findings suggest that myelination by Vangl2 cKO oligodendrocytes results in increased conductivity in the CNS.

FIGURE 6 Loss of Vangl2 expression by oligodendrocytes increases the conductivity of myelinated CNS axons. A representative compound action potential (CAP) recording showing three peaks is shown in (a). The first component is labeled with a black arrowhead, the second with a black arrow, and the third with a gray arrow. The double-headed arrows represent latency, which is measured as the time between the stimulus artifact (asterisk) and the negative peak of each triphasic component. The mean conduction velocity of the three CAP peaks is increased in Vangl2 cKO optic nerve (b; 1st component: WT: 2.47 ± 0.26 m/s, cKO: 3.23 ± 0.23; 2nd component: WT: 1.14 ± 0.11, cKO: 1.37 ± 0.10; third component: WT: 0.57 ± 0.06, cKO: 0.75 ± 0.03, p = .0047). The mean minimum stimulus intensity at which each component of the CAP was first detected was decreased in Vangl2 cKO optic nerve, as shown by representative traces (c, quantification in d; 1st component: WT: 18.9 ± 4.6 μA, cKO: 11.4 ± 2.2; 2nd component: WT: 16.4 ± 1.4, cKO: 12.9 ± 1.8; 3rd component: WT: 42.1 ± 3.2, cKO: 32.1 ± 4.7, p = .0123). Statistical analyses were performed using two-way ANOVA followed by Sidak's multiple comparisons test (b and d). N = 7 nerves from four animals per genotype [Color figure can be viewed at wileyonlinelibrary.com]
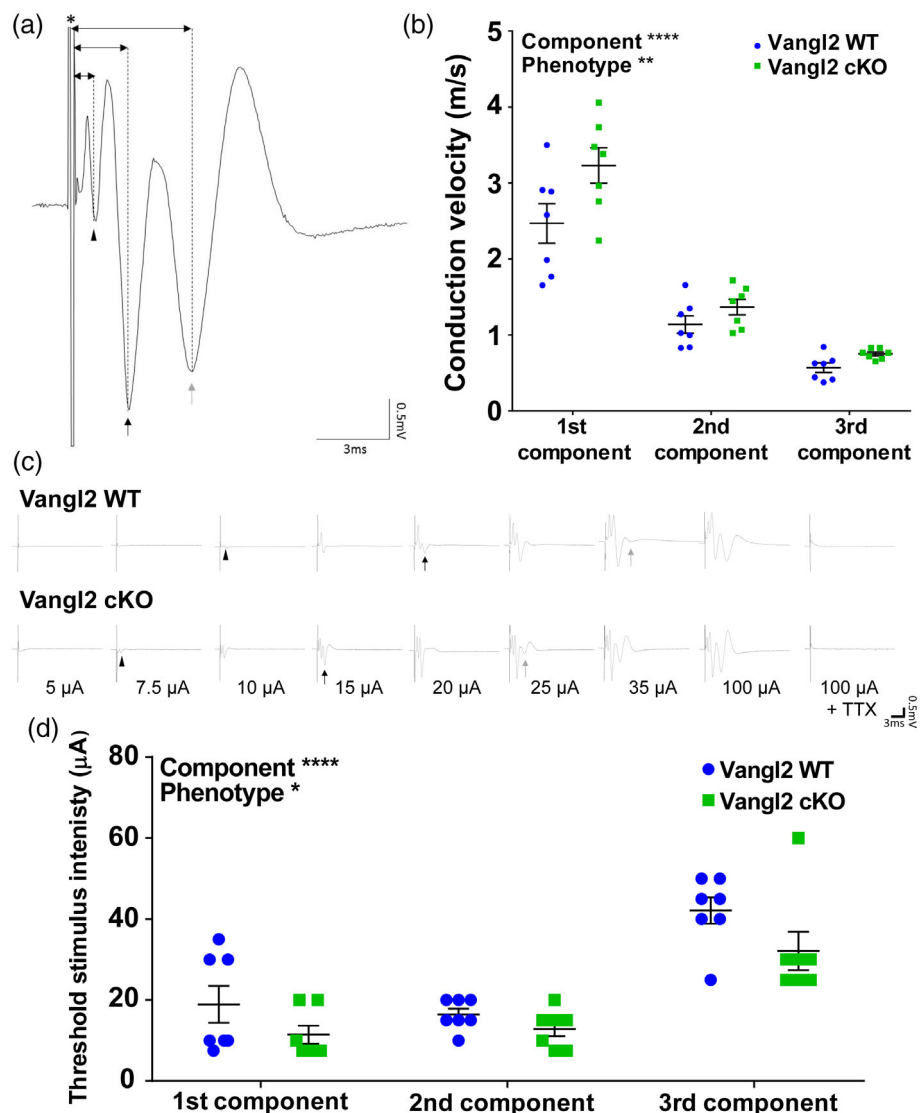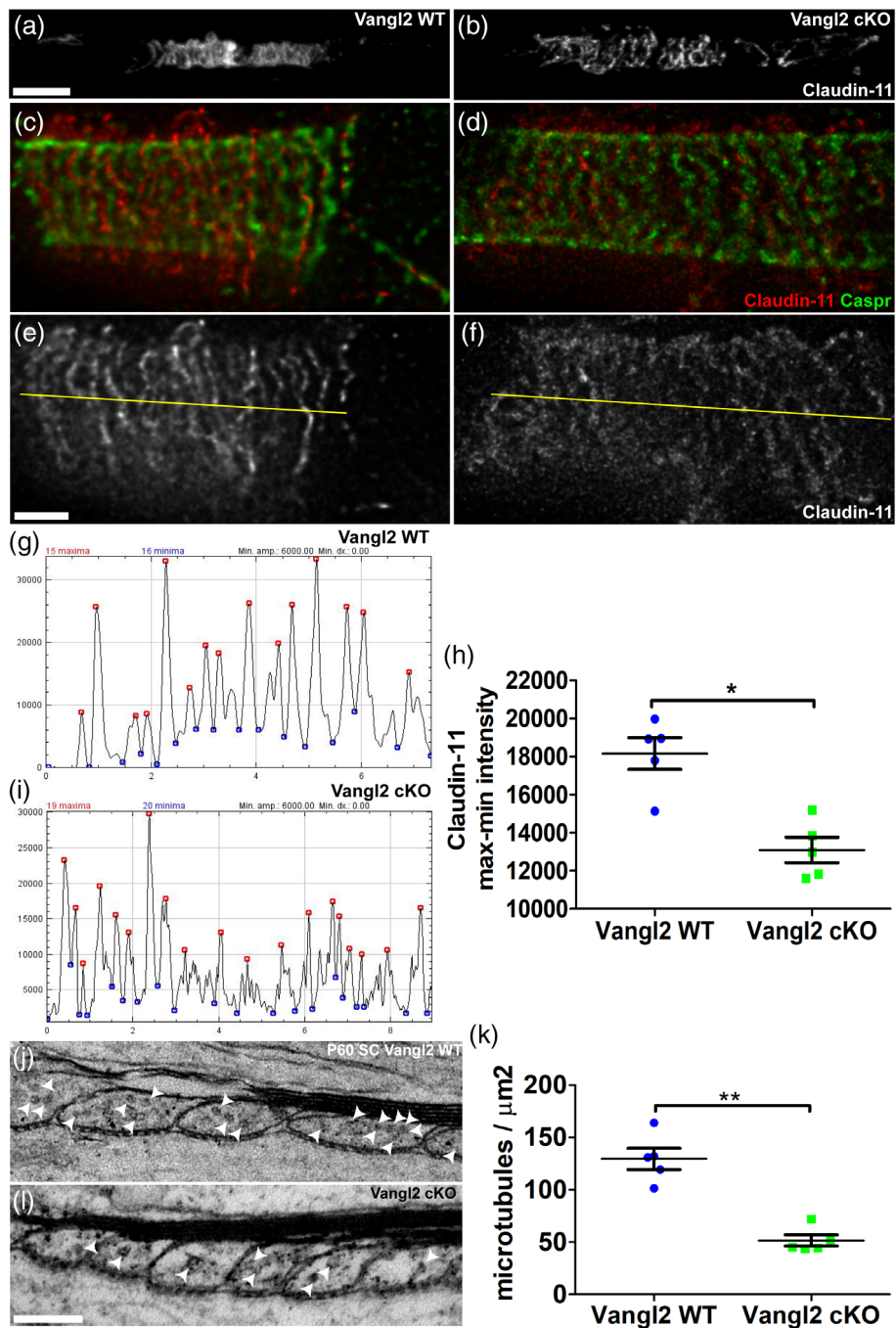
FIGURE 7 Vangl2 controls the distribution of the autotypic tight junction protein Claudin-11 within CNS paranodal myelin. (a–i) Standard and super-resolution gated stimulation emission depletion (gSTED) confocal microscopy revealed altered distribution of Claudin-11 in P60 Vangl2 cKO spinal cord paranodes. The spiral of paranodal oligodendroglial Claudin-11 immunolabeling is loosened and elongated laterally along the axon in teased spinal cord preparations from Vangl2 cKO mice (b) relative to those from Vangl2 WT (a). In Vangl2 cKO paranodes (d and f), the intensity of Claudin-11 distribution (red in c and d, white in e and f) appeared diffuse relative to that observed in wild-type paranodes (c and e). Caspr-immunolabeled axoglial adhesions are shown in green (c and d). When Claudin-11 immunolabeling intensity is plotted across individual paranodes (along the yellow lines in e and f), analysis of intensity maxima (red dots in g and i) and minima (blue dots in g and i) revealed that the difference between maxima and minima was decreased at Vangl2 cKO paranodes (h). (j–l) Microtubule density is reduced in the Vangl2 cKO paranodal spiral. In P60 Vangl2 cKO spinal cord (l), the density of microtubules (white arrowheads) within paranodal loops was decreased relative to that observed in wild-type animals (j, quantification in k; WT: 129.5 ± 10.2 microtubules/μm^2, cKO: 51.6 ± 5.4 microtubules/μm^2, p = .0079). All data are represented as mean ± *SEM*. n = 5 mice per genotype. (c–i) At least 20 paranodes were analyzed per animal. (j–l) At least 50 paranodal loops from at least 10 paranodes were analyzed per animal. Statistical analyses were performed using the Mann–Whitney test. Scale bars: (a and b): 5 μm, (c–f): 1 μm, (j and l): 200 nm [Color figure can be viewed at wileyonlinelibrary.com]

3.6 | Vangl2 regulates the distribution of autotypic adhesion proteins in CNS paranodes

The observed disruption to axonal shape and patterning at nodes of Ranvier and, consequently, on conduction as a result of a "loosened" paranodal spiral following conditional Vangl2 deletion in oligodendroglia raises the question of the mechanism by which Vangl2 "tightens" the spiral. Autotypic tight junctions containing Claudin-11 (Gow et al., 1999) and gap junctions comprised of Connexin-32 (Cx32, Kamasawa et al., 2005) have been reported to bridge loops in CNS paranodal myelin, suggesting that these complexes may be responsible for mediating adhesion between turns of the paranodal spiral. Vangl2 has previously been reported to regulate tight junction organization and claudin-1 localization in uterine luminal epithelium (Yuan et al., 2016), raising the possibility that it may function similarly to localize Claudin-11-containing tight junctions in paranodal myelin. To test this and so provide a mechanism for the loosening of the paranodal spiral in the Vangl2 cKO mice, we imaged Claudin-11 immunolabeling within the loops using super-resolution gSTED confocal microscopy. Standard confocal imaging revealed that the spiral of paranodal Claudin-11 immunolabeling was loosened and extended laterally along the axon in Vangl2 cKO teased spinal cord preparations (Figure 7b) relative to its distribution in wild-type paranodes (Figure 7a). When imaged using gSTED, autotypic Claudin-11-positive tight junctions in wild-type paranodes (red in Figure 7c, white in Figure 7e) appear as a tight spiral surrounding the spiral defined by Caspr-immunolabeled axoglial adhesions (green in Figure 7c,d). In Vangl2 cKO paranodes, by contrast, the Caspr-immunopositive paranodal spiral is still apparent but Claudin-11 immunolabeling appears more diffuse (Figure 7d,f). To quantify this, paranodal intensities were measured by drawing a line through the middle of paranodes (yellow lines in Figure 7e,f), and maximum and minimum intensity levels across each plot (shown as red and blue dots, respectively, in Figure 7g,i) were analyzed. The difference between mean intensity values at maxima and minima were decreased at Vangl2 cKO paranodes (Figure 7h), confirming that Claudin-11 is mislocalized away from the normal band of tight junctions linking the paranodal spiral in Vangl2 cKO CNS.

Studies in epithelial cells show a properly organized microtubule cytoskeleton to be of critical importance to tight junction homeostasis and barrier function (Glotfelty, Zahs, Iancu, Shen, & Hecht, 2014), suggesting a key role for the paranodal microtubules in maintaining the architecture and function of the loops. As Vangl2 regulates microtubule organization and integrity in Sertoli cells of the seminiferous epithelium (Chen, Xiao, Lui, Lee, & Cheng, 2018), we investigated whether the microtubule cytoskeleton within paranodes was also affected by Vangl2 deletion. We found that fewer microtubule cross sections could be observed in Vangl2 cKO spinal cord paranodes at P60 (Figure 7j,l, arrowheads), resulting in a significantly decreased paranodal microtubule density (Figure 7k). This finding is consistent with a mechanism in which the observed mislocalization of Claudin-11, which associates with microtubules through interactions with Sec8 and CASK (Anitei et al., 2006), is a consequence of a disrupted microtubule cytoskeleton in Vangl2 cKO paranodes.

4 | DISCUSSION

Here, we report that the loss of the PCP protein Vangl2 in oligodendrocytes results in disruptions to the microtubule cytoskeleton and autotypic adhesions within the paranodal spiral of noncompact myelin, without perturbing the adhesion of this spiral to the axon. This has three major consequences for the underlying axon. First, a loss of the paranodal barrier resulting in disrupted axonal patterning surrounding nodes of Ranvier. Second, a local increase in paranodal axon diameter. Third, both decreased action potential thresholds and increased conduction velocity in the Vangl2 cKO CNS. These observations reveal that the PCP signaling molecule Vangl2 plays a key role in the sustaining the remarkable architecture of the paranode and so regulating impulse propagation in the CNS. Taken together with our prior work showing that loss of the apico-basal polarity protein Scribble causes the opposite phenotype—loss of axoglial adhesion within the spiral without perturbation of autotypic adhesions—our work suggests that orthogonal axes created by apico-basal and planar polarity pattern the adhesion molecules within the oligodendrocyte cytoplasmic channel to create the paranodal spiral.

This example of subcellular patterning mediated by polarity proteins working at orthogonal axes adds to our understanding as to how the paranodal axoglial adhesions that pattern the axon at nodes of Ranvier are established. The central roles played by the axonal proteins Caspr and Contactin-1 as key constituents of these adhesions and the involvement of proteins such as ankyrin and spectrin family members in linking adhesion proteins to the axonal cytoskeleton has been extensively described in over past 15 years (reviewed by C. Zhang & Rasband, 2016). In comparison, while NFC155 has been demonstrated to be the key oligodendroglial regulator of paranodal axoglial adhesion, relatively little is known about other membrane and cytoskeletal proteins that organize paranodal myelin. The observation that fewer microtubules are present and that Claudin-11 is mislocalized within the paranodal channel in Vangl2 mutants is consistent with a model in which Vangl2 organizes the microtubule cytoskeleton, which is used to transport tight (and potentially other adhesion) junction proteins to their destinations within the paranodal spiral, where they contribute to its stability. Their loss leads to the loosened spiral observed in Vangl2 cKO CNS which, while maintaining contact with the axon, loses its barrier function as axonal nodal and juxtaparanodal complexes become mislocalized laterally along the axon. Loss of Vangl2 cKOs also compromises the organization of noncompact myelin itself, as septin filaments normally confined to the adaxonal internode invade the paranodes.

It is clear, however, that much remains to be learned about the mechanisms that organize the paranodal spiral. The phenotype observed in Vangl2 cKO CNS cannot be explained solely by disruption of Claudin-11. In the Claudin-11 null CNS, disruption to paranodes was not observed and impulse propagation is slowed and not hastened in these animals (Devaux & Gow, 2008; Maheras et al., 2018);

its principal function is believed to be as a diffusion barrier for water and other small molecules (Denninger et al., 2015). One candidate for these additional effects in the Vangl2cKO mice is mislocalization of Cx32, which we were unable to examine by super resolution microscopy due to a lack of suitable antibodies. The primary role of Cx32 gap junctions in myelin is believed to be as a conduit permitting the transport of water, ions and other small molecules between turns of the paranodal spiral, and between abaxonal myelin and astrocytes, allowing for the buffering and recycling of K^+ ions released by neurons (Menichella et al., 2006). However, it has been reported that homotypic Cx32 interaction can drive cell–cell adhesion (Cotrina, Lin, & Nedergaard, 2008), and that enlarged and irregularly shaped paranodal loops are present in the CNS of Cx32 null animals, with neurons in Cx32 mutant displaying hyperexcitability in response to weak stimuli (Sutor, Schmolke, Teubner, Schirmer, & Willecke, 2000). Given that Cx32 gap junctions are found only in oligodendrocytes, and that oligodendrocytes do not appear to form gap junctions with neurons (Rash, Yasumura, Dudek, & Nagy, 2001) these observations could indeed be consistent with this protein playing a role in organizing the paranodal spiral. While mice lacking both it and another oligodendroglial connexin, Cx47, experience a severe CNS phenotype including oligodendrocyte death and CNS demyelination, most likely due to a loss of astrocyte-oligodendrocyte gap junctions (Menichella, Goodenough, Sirkowski, Scherer, & Paul, 2003) Cx32 KO CNS does not show any gross myelin pathology(Scherer et al., 1998). A detailed analysis of myelin organization and axonal patterning at Cx32 KO nodes and paranodes could address the question of whether Cx32 plays an as-yet unidentified role in stabilizing the paranodal spiral in the CNS.

Other adhesion proteins may also play a role in stabilizing the paranodal spiral. In the PNS, E-cadherin is concentrated at adherens junctions between Schwann cell paranodal loops (Fannon et al., 1995). Vangl2 can bind directly to, and control the plasma membrane localization of, both E-cadherin (Nagaoka, Inutsuka, Begum, Bin Hafiz, & Kishi, 2014) and N-cadherin (Nagaoka et al., 2014). While E-cadherin is not expressed in oligodendroglia, N-cadherin is expressed in myelinating oligodendrocytes, where it plays a role in myelin initiation (Schnadelbach, Ozen, Blaschuk, Meyer, & Fawcett, 2001) highlighting this protein as an attractive candidate to mediate adhesion within paranodal spiral in the CNS. Another possible candidate for such a role in the CNS is the transmembrane protein opalin, which has been localized to sites between paranodal loops in CNS myelin (Yoshikawa et al., 2008). However conditional elimination of opalin in oligodendroglia does not affect paranodal organization or conduction, suggesting that it is not essential for the compaction of the paranodal spiral (Yoshikawa et al., 2016). Given the complexity of this structure, it seems likely that Vangl2 regulates the integrity of the paranodal spiral through the downstream actions of several redundant adhesion proteins, both known and yet to be identified. Finally, the possibility that the observed mislocalization of Claudin-11 is a consequence, rather than a cause, of paranodal abnormalities in the Vangl2 cKO CNS cannot be dismissed. Null mutations in the gene encoding the axonal cytoskeletal protein Whirlin also result in paranodal loops trailing into the internode (Green, Yang, Grati, Kachar, & Bhat, 2013),

as well as disrupted paranodal axoglial adhesion and mislocalization of juxtaparanodal K_V channels to paranodes in older animals (Saifetiarova & Bhat, 2019), suggesting that the other causes of disruption to axoglial interaction at the paranode may contribute to the observed trailing-loop phenotype.

A surprising insight gained through our study of the Vangl2 cKO phenotype relates to the ability of paranodal myelin to locally regulate axon diameter. The initial observation in CNS that axonal diameter is greatest at internodes and is decreased at the node of Ranvier and paranodes was made approximately 50 years ago (Hildebrand, 1971), and provides a mechanism to decrease the amount of energy that must be spent to repolarize the membrane following passing of an action potential. Both our own findings and those of Arancibia-Carcamo and colleagues suggest that sodium channel density appears to remain constant as the dimensions of the node of Ranvier change (Arancibia-Carcamo et al., 2017), suggesting that regulation of the amount of nodal membrane present is the primary factor in controlling the number of sodium ions that enter the nodal axon during depolarization. As restoration of membrane resting potential by the Na+/K+ ATPase is responsible for as much as 70% of the energy expenditure of neurons with long-projecting axons in the brain (Howarth, Gleeson, & Attwell, 2012), tightly controlling the dimensions of the node of Ranvier is an important mechanism that ensures that brain energy usage is efficient. However, the mechanism underlying nodal diameter reduction remains unknown. It has been observed in PNS that in cross sections of internodal regions of myelinated axons, neurofilaments are relatively spread out, while they are more densely packed together at paranodes (Price, Lasek, & Katz, 1990) suggesting an external compressive force (Price, Lasek, & Katz, 1993). In the PNS, it was observed that a dense actin cytoskeleton encircles the paranodal axon, leading to the hypothesis that actin contractility within the Schwann cell generates force that squeezes the paranodal axon (Zimmermann, 1996). Vangl2 has a previously reported role in generating contractile force through regulation of the actin cytoskeleton during gastrulation (Ossipova, Chuykin, Chu, & Sokol, 2015), but as filamentous actin is largely absent from CNS myelin (Zuchero et al., 2015) any such compression would have to be driven by an actin-independent process. One possible interpretation of our findings is that increased paranodal axon diameter is consistent with an inability of the paranodal spiral to "lock" by adhesion between loops at Vangl2 cKO CNS paranodes, leading to relaxation and lengthening of the spiral and an inability to squeeze the enlarging axon at paranodes as radial growth proceeds between P14 and P60. The presence of a compressive action of the paranodal spiral on the axon has not been proven at CNS or PNS nodes, however, and further investigation will be required to determine the mechanism by which Vangl2 regulates paranodal axon diameter.

We observed in the *Vangl2* cKO mice that the length of the Na_V-immunopositive domain was increased, extending into the paranode even though the length of the node as measured by electron microscopy was not altered. This lengthening presumably occurs through spiral diffusion of the channels along the widened areas of axon membrane created between turns of the loosened paranodal loops—the

so-called "pathway 3" described by Mierzwa in 2010 (Mierzwa, Shroff, & Rosenbluth, 2010). This in turn may explain why nerves lacking oligodendroglial Vangl2 expression show increased conduction velocities despite internodal lengths in Vangl2 cKO teased spinal cord fibers not varying significantly from wild-type (data not shown). Mathematical modeling of conduction along myelinated CNS axons predicts that the length of nodes of Ranvier (and therefore the length of the Na_V-immunopositive domain in normal mice) is a key parameter that influences conduction velocity (Arancibia-Carcamo et al., 2017). Using the computer model published by Arancibia-Carcamo et al., using our measured length of the Na_V-immunopositive domain in the *Vangl2* cKO mice (Figure 4h) as the nodal length predicts an increase in conduction velocity (Values used: Nodal diameter: WT: 0.88 μm, cKO: 0.88; Nodal length: WT: 1.95 μm, cKO: 3.18 μm; Internodal length: WT: 576.5 μm, cKO: 500.6 μm; Internodal diameter: WT: 3.45 μm, cKO: 3.75 μm; g-ratio: WT: 0.759, cKO: 0.753; Predicted conduction velocity: WT: 11.85 m/s, cKO: 14.20 m/s), consistent with the results of our electrophysiological studies. A key assumption of this model, however, is that the density of sodium channels at the nodal plasma membrane is held constant. Indeed, we found that no significant difference in the mean intensity of nodal Na_V immunofluorescence could be observed in Vangl2 cKO teased spinal cord at P60, suggesting that the functionally longer nodes of Ranvier in the Vangl2 cKO contain more voltage-gated sodium channels than do those in wild-type CNS. Implicit in our assumption is that the entire sodium channel domain (and not just the region of bare axon between adjacent myelin segments) contributes to conduction in Vangl2 cKO, with the sodium channels mislocalized into paranodal regions in these animals accessible and actively contributing to depolarization.

Our results showing increased conduction velocity with loss of loop–loop adhesion differs from that reported for animals lacking another paranodal autotypic adhesion molecule, JAM-C (Scheiermann et al., 2007). Here decreased conduction is seen in the PNS of JAM-C deficient mice. However, a deficiency of JAM-C causes a loss of both loop–loop and loop-axon adhesion, as shown in figs. 2B and S4D of that paper. We suggest that there will be a much greater perturbation of the paranodal sealing required for saltatory conduction resulting from loss of adhesion between loops and the underlying axon than from a loop–loop defect, and that this loss of sealing then dominates the electrophysiological phenotype.

A predicted consequence of an increased number of sodium channels at Vangl2 cKO nodes of Ranvier would be a corresponding increase in the amount of energy required to repolarize the membrane following passing of an action potential. Interestingly and consistent with this, we observed that an increased proportion of nodes of Ranvier in Vangl2 cKO P60 spinal cord contained mitochondria compared to wild-type nodes (data not shown), which could represent a response to this increased metabolic demand of the Na^+/K^+ ATPase as has been observed in the peripheral nervous system (PNS,C. L. Zhang, Ho, Kintner, Sun, & Chiu, 2010). Increased energy demand by axons could also explain why myelin sheaths in P60 Vangl2 cKO spinal cord contain significantly more internodal Schmidt-Lanterman incisure-like myelinic channels (data not shown), as these structures are thought to play a key

role in delivering metabolic support from the oligodendrocyte to the axon (Philips & Rothstein, 2017).

Finally, our finding that Vangl2 is a key regulator of paranodal architecture also has important implications for myelin pathology and plasticity. Paranodal loosening occurs with CNS aging (Hinman et al., 2006) and elongation of paranodes has been observed in regions of the brain that have undergone remyelination in multiple sclerosis patients (Howell et al., 2006). The similarity of these phenotypes with those we see here suggests that Vangl2 may be compromised in aging or disease. Such a conclusion is potentially important, as a possible consequence of "looser" paranodal assembly could be increased susceptibility of the myelin sheath to age-related demyelination, or to further damage following remyelination, at least in part due to the presence of circulating antibodies in the sera of individuals suffering from multiple sclerosis recognizing paranodal epitopes that are normally inaccessible (Mathey et al., 2007). This could for example provide an explanation for why MS lesions often reoccur in regions where lesions have already occurred (Prineas et al., 1993).

CONFLICT OF INTEREST

The authors declare no competing interests.

DATA AVAILABILITY STATEMENT

The data that support the findings of this study are available from the corresponding author upon reasonable request.

ORCID

Andrew A. Jarjour https://orcid.org/0000-0002-1550-1778

REFERENCES

Amor, V., Zhang, C., Vainshtein, A., Zhang, A., Zollinger, D. R., Eshed-Eisenbach, Y., ... Peles, E. (2017). The paranodal cytoskeleton clusters Na(+) channels at nodes of Ranvier. *eLife*, 6, e21392. https://doi.org/10.7554/eLife.21392

Anitei, M., Ifrim, M., Ewart, M. A., Cowan, A. E., Carson, J. H., Bansal, R., & Pfeiffer, S. E. (2006). A role for Sec8 in oligodendrocyte morphological differentiation. *Journal of Cell Science*, 119(Pt. 5), 807–818.

Arancibia-Carcamo, I. L., Ford, M. C., Cossell, L., Ishida, K., Tohyama, K., & Attwell, D. (2017). Node of Ranvier length as a potential regulator of myelinated axon conduction speed. *Elife*, 6, e23329. https://doi.org/10.7554/eLife.23329

Bhat, M. A., Rios, J. C., Lu, Y., Garcia-Fresco, G. P., Ching, W., St Martin, M., ... Bellen, H. J. (2001). Axon-glia interactions and the domain organization of myelinated axons requires neurexin IV/-Caspr/Paranodin. *Neuron*, 30(2), 369–383.

Bilder, D., & Perrimon, N. (2000). Localization of apical epithelial determinants by the basolateral PDZ protein Scribble. *Nature*, 403(6770), 676–680.

Boison, D., Bussow, H., Durso, D., Muller, H. W., & Stoffel, W. (1995). Adhesive properties of proteolipid protein are responsible for the compaction of Cns myelin sheaths. *Journal of Neuroscience*, 15(8), 5502–5513.

Campanale, J. P., Sun, T. Y., & Montell, D. J. (2017). Development and dynamics of cell polarity at a glance. *Journal of Cell Science*, 130(7), 1201–1207. https://doi.org/10.1242/jcs.188599

Charles, P., Tait, S., Faivre-Sarrailh, C., Barbin, G., Gunn-Moore, F., Denisenko-Nehrbass, N., ... Lubetzki, C. (2002). Neurofascin is a glial receptor for the paranodin/Caspr-contactin axonal complex at the axoglial junction. *Current Biology*, 12(3), 217–220.

Chen, H., Xiao, X., Lui, W. Y., Lee, W. M., & Cheng, C. Y. (2018). Vangl2 regulates spermatid planar cell polarity through microtubule (MT)-based cytoskeleton in the rat testis. *Cell Death & Disease*, 9(3), 340. https://doi.org/10.1038/s41419-018-0339-x

Cotrina, M. L., Lin, J. H., & Nedergaard, M. (2008). Adhesive properties of connexin hemichannels. *Glia*, 56(16), 1791–1798. https://doi.org/10.1002/glia.20728

Courbard, J. R., Djiane, A., Wu, J., & Mlodzik, M. (2009). The apical/basal-polarity determinant Scribble cooperates with the PCP core factor Stbm/Vang and functions as one of its effectors. *Developmental Biology*, 333(1), 67–77. https://doi.org/10.1016/j.ydbio.2009.06.024

Denninger, A. R., Breglio, A., Maheras, K. J., LeDuc, G., Cristiglio, V., Deme, B., ... Kirschner, D. A. (2015). Claudin-11 tight junctions in myelin are a barrier to diffusion and lack strong adhesive properties. *Biophysical Journal*, 109(7), 1387–1397. https://doi.org/10.1016/j.bpj.2015.08.012

Devaux, J., & Gow, A. (2008). Tight junctions potentiate the insulative properties of small CNS myelinated axons. *Journal of Cell Biology*, 183(5), 909–921. https://doi.org/10.1083/jcb.200808034

Dos-Santos Carvalho, S., Moreau, M. M., Hien, Y. E., Garcia, M., Aubailly, N., Henderson, D. J., ... Montcouquiol, M. (2020). Vangl2 acts at the interface between actin and N-cadherin to modulate mammalian neuronal outgrowth. *eLife*, 9, e51822. https://doi.org/10.7554/eLife.51822

Fannon, A. M., Sherman, D. L., Ilyina-Gragerova, G., Brophy, P. J., Friedrich, V. L., Jr., & Colman, D. R. (1995). Novel E-cadherin-mediated adhesion in peripheral nerve: Schwann cell architecture is stabilized by autotypic adherens junctions. *Journal of Cell Biology*, 129(1), 189–202.

Ferreira, T., Hiner, M., Rueden, C., Miura, K., Eglinger, J., & Chef, B. (2017). *tferr/Scripts: BAR 1.5.1* (Version 1.51). http://doi.org/10.5281/zenodo.495245.

Foster, R. E., Connors, B. W., & Waxman, S. G. (1982). Rat optic nerve: Electrophysiological, pharmacological and anatomical studies during development. *Brain Research*, 255(3), 371–386.

Fünfschilling, U., Supplie, L., Mahad, D., Boretius, S., Saab, A., Edgar, J., ... Nave, K.-A. (2012). Glycolytic oligodendrocytes maintain myelin and long-term axonal integrity. *Nature*, 485(7399), 517–538. https://doi.org/10.1038/nature11007

Glotfelty, L. G., Zahs, A., Iancu, C., Shen, L., & Hecht, G. A. (2014). Microtubules are required for efficient epithelial tight junction homeostasis and restoration. *American Journal of Physiology. Cell Physiology*, 307(3), C245–C254. https://doi.org/10.1152/ajpcell.00336.2013

Gow, A., Southwood, C. M., Li, J. S., Pariali, M., Riordan, G. P., Brodie, S. E., ... Lazzarini, R. A. (1999). CNS myelin and sertoli cell tight junction strands are absent in Osp/claudin-11 null mice. *Cell*, 99(6), 649–659.

Green, J. A., Yang, J., Grati, M., Kachar, B., & Bhat, M. A. (2013). Whirlin, a cytoskeletal scaffolding protein, stabilizes the paranodal region and axonal cytoskeleton in myelinated axons. *BMC Neuroscience*, 14, 96. https://doi.org/10.1186/1471-2202-14-96

Hildebrand, C. (1971). Ultrastructural and light-microscopic studies of the nodal region in large myelinated fibres of the adult feline spinal cord white matter. *Acta Physiologica Scandinavica. Supplementum*, 364, 43–79.

Hildebrand, C., & Skoglund, S. (1971). Calibre spectra of some fibre tracts in the feline central nervous system during postnatal development. *Acta Physiologica Scandinavica. Supplementum*, 364, 5–41.

Hinman, J. D., Peters, A., Cabral, H., Rosene, D. L., Hollander, W., Rasband, M. N., & Abraham, C. R. (2006). Age-related molecular reorganization at the node of Ranvier. *Journal of Comparative Neurology*, 495(4), 351–362. https://doi.org/10.1002/cne.20886

Howarth, C., Gleeson, P., & Attwell, D. (2012). Updated energy budgets for neural computation in the neocortex and cerebellum. *Journal of Cerebral Blood Flow and Metabolism*, 32(7), 1222–1232. https://doi.org/10.1038/jcbfm.2012.35

Howell, O. W., Palser, A., Polito, A., Melrose, S., Zonta, B., Scheiermann, C., ... Reynolds, R. (2006). Disruption of neurofascin localization reveals early changes preceding demyelination and remyelination in multiple sclerosis. *Brain*, 129(Pt 12), 3173–3185.

Huxley, A. F., & Stampfli, R. (1949). Evidence for saltatory conduction in peripheral myelinated nerve fibres. *Journal of Physiology*, 108(3), 315–339.

Jarjour, A. A., Boyd, A., Dow, L. E., Holloway, R. K., Goebbels, S., Humbert, P. O., ... ffrench-Constant, C. (2015). The polarity protein Scribble regulates myelination and remyelination in the central nervous system. *PLoS Biology*, 13(3), e1002107. https://doi.org/10.1371/journal.pbio.1002107

Kamasawa, N., Sik, A., Morita, M., Yasumura, T., Davidson, K. G., Nagy, J. I., & Rash, J. E. (2005). Connexin-47 and connexin-32 in gap junctions of oligodendrocyte somata, myelin sheaths, paranodal loops and Schmidt-Lanterman incisures: Implications for ionic homeostasis and potassium siphoning. *Neuroscience*, 136(1), 65–86.

Lappe-Siefke, C., Goebbels, S., Gravel, M., Nicksch, E., Lee, J., Braun, P. E., ... Nave, K. A. (2003). Disruption of Cnp1 uncouples oligodendroglial functions in axonal support and myelination. *Nature Genetics*, 33(3), 366–374.

Lee, Y., Morrison, B. M., Li, Y., Lengacher, S., Farah, M. H., Hoffman, P. N., ... Rothstein, J. D. (2012). Oligodendroglia metabolically support axons and contribute to neurodegeneration. *Nature*, 487(7408), 443–448. https://doi.org/10.1038/nature11314

Leung, V., Iliescu, A., Jolicoeur, C., Gravel, M., Apuzzo, S., Torban, E., ... Gros, P. (2016). The planar cell polarity protein Vangl2 is required for retinal axon guidance. *Developmental Neurobiology*, 76(2), 150–165. https://doi.org/10.1002/dneu.22305

Liu, C., Lin, C., Whitaker, D. T., Bakeri, H., Bulgakov, O. V., Liu, P., ... Swaroop, A. (2013). Prickle1 is expressed in distinct cell populations of the central nervous system and contributes to neuronal morphogenesis. *Human Molecular Genetics*, 22(11), 2234–2246. https://doi.org/10.1093/hmg/ddt075

Maheras, K. J., Peppi, M., Ghoddoussi, F., Galloway, M. P., Perrine, S. A., & Gow, A. (2018). Absence of Claudin 11 in CNS myelin perturbs behavior and neurotransmitter levels in mice. *Scientific Reports*, 8(1), 3798. https://doi.org/10.1038/s41598-018-22047-9

Mathey, E. K., Derfuss, T., Storch, M. K., Williams, K. R., Hales, K., Woolley, D. R., ... Linington, C. (2007). Neurofascin as a novel target for autoantibody-mediated axonal injury. *Journal of Experimental Medicine*, 204(10), 2363–2372. https://doi.org/10.1084/jem.20071053

Menichella, D. M., Goodenough, D. A., Sirkowski, E., Scherer, S. S., & Paul, D. L. (2003). Connexins are critical for normal myelination in the CNS. *Journal of Neuroscience*, 23(13), 5963–5973.

Menichella, D. M., Majdan, M., Awatramani, R., Goodenough, D. A., Sirkowski, E., Scherer, S. S., & Paul, D. L. (2006). Genetic and physiological evidence that oligodendrocyte gap junctions contribute to spatial buffering of potassium released during neuronal activity. *Journal of Neuroscience*, 26(43), 10984–10991. https://doi.org/10.1523/JNEUROSCI.0304-06.2006

Mierzwa, A., Shroff, S., & Rosenbluth, J. (2010). Permeability of the paranodal junction of myelinated nerve fibers. *Journal of Neuroscience*, 30

(47), 15962–15968. https://doi.org/10.1523/JNEUROSCI.4047-10. 2010

Montcouquiol, M., Rachel, R. A., Lanford, P. J., Copeland, N. G., Jenkins, N. A., & Kelley, M. W. (2003). Identification of Vangl2 and Scrb1 as planar polarity genes in mammals. *Nature*, *423*(6936), 173–177.

Nagaoka, T., Inutsuka, A., Begum, K., Bin Hafiz, K., & Kishi, M. (2014). Vangl2 regulates E-cadherin in epithelial cells. *Scientific Reports*, *4*, 6940. https://doi.org/10.1038/srep06940

Nagaoka, T., Ohashi, R., Inutsuka, A., Sakai, S., Fujisawa, N., Yokoyama, M., … Kishi, M. (2014). The Wnt/planar cell polarity pathway component Vangl2 induces synapse formation through direct control of N-cadherin. *Cell Reports*, *6*(5), 916–927. https://doi.org/10.1016/j.celrep. 2014.01.044

Okerlund, N. D., Stanley, R. E., & Cheyette, B. N. (2016). The planar cell polarity transmembrane protein Vangl2 promotes dendrite, spine and glutamatergic synapse formation in the mammalian forebrain. *Molecular Neuropsychiatry*, *2*(2), 107–114. https://doi.org/10.1159/000446778

Ossipova, O., Chuykin, I., Chu, C. W., & Sokol, S. Y. (2015). Vangl2 cooperates with Rab11 and myosin V to regulate apical constriction during vertebrate gastrulation. *Development*, *142*(1), 99–107. https://doi.org/10.1242/dev.111161

Patzig, J., Erwig, M. S., Tenzer, S., Kusch, K., Dibaj, P., Mobius, W., … Werner, H. B. (2016). Septin/anillin filaments scaffold central nervous system myelin to accelerate nerve conduction. *eLife*, *5*, e17119. https://doi.org/10.7554/eLife.17119

Philips, T., & Rothstein, J. D. (2017). Oligodendroglia: Metabolic supporters of neurons. *Journal of Clinical Investigation*, *127*(9), 3271–3280. https://doi.org/10.1172/JCI90610

Price, R. L., Lasek, R. J., & Katz, M. J. (1990). Internal axonal cytoarchitecture is shaped locally by external compressive forces. *Brain Research*, *530*(2), 205–214.

Price, R. L., Lasek, R. J., & Katz, M. J. (1993). Neurofilaments assume a less random architecture at nodes and in other regions of axonal compression. *Brain Research*, *607*(1–2), 125–133.

Prineas, J. W., Barnard, R. O., Revesz, T., Kwon, E. E., Sharer, L., & Cho, E. S. (1993). Multiple sclerosis. Pathology of recurrent lesions. *Brain*, *116*(Pt. 3), 681–693.

Ramsbottom, S. A., Sharma, V., Rhee, H. J., Eley, L., Phillips, H. M., Rigby, H. F., … Henderson, D. J. (2014). Vangl2-regulated polarisation of second heart field-derived cells is required for outflow tract lengthening during cardiac development. *PLoS Genetics*, *10*(12), e1004871. https://doi.org/10.1371/journal.pgen.1004871

Rash, J. E., Yasumura, T., Dudek, F. E., & Nagy, J. I. (2001). Cell-specific expression of connexins and evidence of restricted gap junctional coupling between glial cells and between neurons. *Journal of Neuroscience*, *21*(6), 1983–2000.

Rios, J. C., Melandez-Vasquez, C. V., Einheber, S., Lustig, M., Grumet, M., Hemperly, J., … Salzer, J. L. (2000). Contactin-associated protein (Caspr) and contactin form a complex that is targeted to the paranodal junctions during myelination. *Journal of Neuroscience*, *20*(22), 8354–8364.

Saifetiarova, J., & Bhat, M. A. (2019). Ablation of cytoskeletal scaffolding proteins, Band 4.1B and Whirlin, leads to cerebellar purkinje axon pathology and motor dysfunction. *Journal of Neuroscience Research*, *97*(3), 313–331. https://doi.org/10.1002/jnr.24352

Sanchez, I., Hassinger, L., Paskevich, P. A., Shine, H. D., & Nixon, R. A. (1996). Oligodendroglia regulate the regional expansion of axon caliber and local accumulation of neurofilaments during development independently of myelin formation. *Journal of Neuroscience*, *16*(16), 5095–5105.

Sargiannidou, I., Vavlitou, N., Aristodemou, S., Hadjisavvas, A., Kyriacou, K., Scherer, S. S., & Kleopa, K. A. (2009). Connexin32 mutations cause loss of function in Schwann cells and oligodendrocytes leading to PNS and CNS myelination defects. *Journal of Neuroscience*, *29*(15), 4736–4749. https://doi.org/10.1523/JNEUROSCI.0325-09.2009

Scheiermann, C., Meda, P., Aurrand-Lions, M., Madani, R., Yiangou, Y., Coffey, P., … Nourshargh, S. (2007). Expression and function of junctional adhesion molecule-C in myelinated peripheral nerves. *Science*, *318*(5855), 1472–1475. https://doi.org/10.1126/science. 1149276

Scherer, S. S., Xu, Y. T., Nelles, E., Fischbeck, K., Willecke, K., & Bone, L. J. (1998). Connexin32-null mice develop demyelinating peripheral neuropathy. *Glia*, *24*(1), 8–20.

Schindelin, J., Arganda-Carreras, I., Frise, E., Kaynig, V., Longair, M., Pietzsch, T., … Cardona, A. (2012). Fiji: An open-source platform for biological-image analysis. *Nature Methods*, *9*(7), 676–682. https://doi.org/10.1038/nmeth.2019

Schnadelbach, O., Ozen, I., Blaschuk, O. W., Meyer, R. L., & Fawcett, J. W. (2001). N-cadherin is involved in axon-oligodendrocyte contact and myelination. *Molecular and Cellular Neurosciences*, *17*(6), 1084–1093. https://doi.org/10.1006/mcne.2001.0961

Simons, M., Snaidero, N., & Aggarwal, S. (2012). Cell polarity in myelinating glia: From membrane flow to diffusion barriers. *Biochimica et Biophysica Acta*, *1821*(8), 1146–1153. https://doi.org/10.1016/j.bbalip. 2012.01.011

Sun, S. D., Purdy, A. M., & Walsh, G. S. (2016). Planar cell polarity genes Frizzled3a, Vangl2, and Scribble are required for spinal commissural axon guidance. *BMC Neuroscience*, *17*(1), 83. https://doi.org/10.1186/s12868-016-0318-z

Sutor, B., Schmolke, C., Teubner, B., Schirmer, C., & Willecke, K. (2000). Myelination defects and neuronal hyperexcitability in the neocortex of connexin 32-deficient mice. *Cerebral Cortex*, *10*(7), 684–697.

Tasaki, I., & Takeuchi, T. (1942). Weitere Studien über den Aktionsstrom der markhaltigen Nervenfaser und über die elektrosaltatorische Übertragung des Nervenimpulses. *Pflüger's Archiv für die gesamte Physiologie des Menschen und der Tiere*, *245*(5), 764–782. https://doi.org/10.1007/bf01755237

Thakar, S., Wang, L., Yu, T., Ye, M., Onishi, K., Scott, J., … Zou, Y. (2017). Evidence for opposing roles of Celsr3 and Vangl2 in glutamatergic synapse formation. *Proceedings of the National Academy of Sciences of the United States of America*, *114*(4), E610–E618. https://doi.org/10.1073/pnas.1612062114

Yates, L. L., Schnatwinkel, C., Hazelwood, L., Chessum, L., Paudyal, A., Hilton, H., … Dean, C. H. (2013). Scribble is required for normal epithelial cell–cell contacts and lumen morphogenesis in the mammalian lung. *Developmental Biology*, *373*(2), 267–280. https://doi.org/10.1016/j.ydbio.2012.11.012

Yoshikawa, F., Sato, Y., Tohyama, K., Akagi, T., Furuse, T., Sadakata, T., … Furuichi, T. (2016). Mammalian-specific central myelin protein opalin is redundant for normal myelination: Structural and behavioral assessments. *PLoS One*, *11*(11), e0166732. https://doi.org/10.1371/journal.pone.0166732

Yoshikawa, F., Sato, Y., Tohyama, K., Akagi, T., Hashikawa, T., Nagakura-Takagi, Y., … Furuichi, T. (2008). Opalin, a transmembrane sialylglycoprotein located in the central nervous system myelin paranodal loop membrane. *Journal of Biological Chemistry*, *283*(30), 20830–20840. https://doi.org/10.1074/jbc.M801314200

Yuan, J., Cha, J., Deng, W., Bartos, A., Sun, X., Ho, H. H., … Dey, S. K. (2016). Planar cell polarity signaling in the uterus directs appropriate positioning of the crypt for embryo implantation. *Proceedings of the National Academy of Sciences of the United States of America*, *113*(50), E8079–E8088. https://doi.org/10.1073/pnas.1614946113

Zhang, C., & Rasband, M. N. (2016). Cytoskeletal control of axon domain assembly and function. *Current Opinion in Neurobiology*, *39*, 116–121. https://doi.org/10.1016/j.conb.2016.05.001

Zhang, C. L., Ho, P. L., Kintner, D. B., Sun, D., & Chiu, S. Y. (2010). Activity-dependent regulation of mitochondrial motility by calcium and Na/K-ATPase at nodes of Ranvier of myelinated nerves. *Journal of*

Neuroscience, *30*(10), 3555–3566. https://doi.org/10.1523/JNEUROSCI.4551-09.2010

Zilkha-Falb, R., Gurevich, M., Hanael, E., & Achiron, A. (2017). Prickle1 as positive regulator of oligodendrocyte differentiation. *Neuroscience*, *364*, 107–121. https://doi.org/10.1016/j.neuroscience.2017.09.018

Zimmermann, H. (1996). Accumulation of synaptic vesicle proteins and cytoskeletal specializations at the peripheral node of Ranvier. *Microscopy Research and Technique*, *34*(5), 462–473.

Zollinger, D. R., Baalman, K. L., & Rasband, M. N. (2015). The ins and outs of polarized axonal domains. *Annual Review of Cell and Developmental Biology*, *31*, 647–667. https://doi.org/10.1146/annurev-cellbio-100913-013107

Zonta, B., Tait, S., Melrose, S., Anderson, H., Harroch, S., Higginson, J., … Brophy, P. J. (2008). Glial and neuronal isoforms of Neurofascin have distinct roles in the assembly of nodes of Ranvier in the central nervous system. *Journal of Cell Biology*, *181*(7), 1169–1177.

Zuchero, J. B., Fu, M. M., Sloan, S. A., Ibrahim, A., Olson, A., Zaremba, A., … Barres, B. A. (2015). CNS myelin wrapping is driven by actin disassembly. *Developmental Cell*, *34*(2), 152–167. https://doi.org/10.1016/j.devcel.2015.06.011

SUPPORTING INFORMATION

Additional supporting information may be found online in the Supporting Information section at the end of this article.